Dynamics of outgassing and plume transport revealed by proximal Unmanned Aerial System (UAS) measurements at Volcán Villarrica, Chile

Emma J. Liu[1*], Kieran Wood[2], Emily Mason[1], Marie Edmonds[1], Alessandro Aiuppa[3,4], Gaetano Giudice[4], Marcello Bitetto[3], Vincenzo Francofonte[4], Steve Burrow[2], Thomas Richardson[2], Matthew Watson[5], Tom D. Pering[6], Thomas C. Wilkes[6], Andrew J. S. McGonigle[4,6,7], Gabriela Velasquez[8], Carlos Melgarejo[8], Claudia Bucarey[8].

[1]Department of Earth Sciences, University of Cambridge, Downing Street, Cambridge, U.K.
*(ejl54@cam.ac.uk)
[2]Department of Aerospace Engineering, University of Bristol, Queens Building, Bristol, U.K.
[3]Dipartimento DiSTeM, Università di Palermo, Palermo, Italy.
[4]Istituto Nazionale di Geofisica e Vulcanologia, Sezione di Palermo, Palermo, Italy.
[5]School of Earth Sciences, University of Bristol, Wills Memorial Building, U.K.
[6]University of Sheffield, Department of Geography, Winter Street, U.K.
[7]School of Geosciences, University of Sydney, Sydney NSW2006, Australia.
[8]Observatorio Volcanológico de los Andes del Sur (OVDAS), Red Nacional de Vigilancia Volcánica (RNVV), Servicio Nacional de Geología y Minería, Temuco, Chile.

Abstract

Volcanic gas emissions are intimately linked to the dynamics of magma ascent and outgassing, and, on geological timescales, constitute an important source of volatiles to the Earth's atmosphere. Measurements of gas composition and flux are therefore critical to both volcano monitoring and to determining the contribution of volcanoes to global geochemical cycles. However, significant gaps remain in our global inventories of volcanic emissions, (particularly for CO_2, which requires proximal sampling of a concentrated plume) for those volcanoes where the near-vent region is hazardous or inaccessible. Unmanned Aerial Systems (UAS) provide a robust and effective solution to proximal sampling of dense volcanic plumes in extreme volcanic environments. Here, we present gas compositional data acquired using a gas sensor payload aboard a UAS flown at Volcán Villarrica, Chile. We compare UAS-derived gas timeseries to simultaneous crater rim multi-GAS data and UV camera imagery to investigate early plume evolution. SO_2 concentrations measured in the young proximal plume exhibit periodic variations that are well-correlated with the concentrations of other species. By combining molar gas ratios (CO_2/SO_2 = 1.48–1.68, H_2O/SO_2 = 67–75 and H_2O/CO_2 = 45–51) with the SO_2 flux (142 ± 17 t/day) from UV camera images, we derive CO_2 and H_2O fluxes of ~150 t/day and ~2850 t/day, respectively. We observe good agreement between

This article has been accepted for publication and undergone full peer review but has not been through the copyediting, typesetting, pagination and proofreading process which may lead to differences between this version and the Version of Record. Please cite this article as doi: 10.1029/2018GC007692

time-averaged molar gas ratios obtained from simultaneous UAS- and ground-based multi-GAS acquisitions. However, the UAS measurements made in the young, less diluted plume reveal additional short-term periodic structure that reflects active degassing through discrete, audible gas exhalations.

Introduction

The gases released by volcanoes at the Earth's surface are a window into the magmatic systems beneath. Abrupt changes in gas composition have been shown to occur immediately prior to large 'paroxysmal' eruptions at several arc volcanoes worldwide, with gas ratios such as CO_2/SO_2 identified in hindsight as timely forecasts of shifts in eruptive behaviour (Shinohara et al., 2005, 2008; Aiuppa et al., 2007, 2010a, b; 2017b; Werner et al., 2013; de Moor et al., 2016). Cyclical variations in gas flux, particularly when cross-correlated with other monitoring parameters such as seismicity or ground deformation, provide critical insight into the mechanisms governing the timescales of recurrent eruptive activity (Werner et al., 2008; Nicholson et al., 2013, Tamburello et al., 2013, Odbert et al., 2014, Flower and Carn, 2015, Ilanko et al., 2015) and the data required to test hypotheses generated by numerical conduit models (e.g., Costa et al., 2007a, b). On geological timescales, quantification of degassing budgets on a regional- or global-scale offers important constraints on volatile cycling through the Earth system (Aiuppa et al., 2017a; Mason et al., 2017). However, there remain significant gaps in our global inventories of volcanic gas emissions, particularly for CO_2 and other species which usually require proximal sampling of a concentrated plume, for those volcanoes where the near-vent region is hazardous or inaccessible.

Measurements of volcanic gas emissions can be either direct or remote. Direct measurements requiring placement of an instrument close to the vent source by volcanologists are hazardous to acquire and the instruments may often be destroyed during eruptions (e.g., Aiuppa et al., 2017b). However, the high gas concentrations and limited atmospheric entrainment in young, proximal plumes yield high quality data that record faithfully primary degassing processes at a temporal resolution approaching that of geophysical data ($\leq$ 1 Hz). Remote measurements, such as can be acquired using imaging or spectral techniques (e.g., UV/IR-cameras and COSPEC/scanning-DOAS/FlySpec/mobile-DOAS, respectively), are typically performed several kilometres from the volcanic gas source and therefore pose little to no direct risk to volcanologists or equipment (e.g., Moffat and Millán 1971; Oppenheimer et al., 1998; Weibring et al., 1998; Edmonds et al., 2003;

McGonigle et al., 2002, 2003; Galle et al., 2003; Horton et al., 2006; Mori and Burton, 2006; Bluth et al., 2007; Holland et al., 2011; Tamburello et al., 2012, 2013; Wilkes et al., 2016; Platt et al., 2018). Note that, although significant progress has been made in the use of LIght Detection And Ranging (LIDAR) for remote sensing of CO_2 (Santoro et al., 2017), SO_2 is currently the only gas species able to be measured routinely by remote methods due to its strong absorption at UV wavelengths and the negligible concentration in ambient air. Globally, volcanic SO_2 emissions are routinely monitored from space using satellite-based instrumentation (such as the Ozone Monitoring Instrument, OMI), or by ground-based networks at specific volcanoes (for example, the NOVAC network; Galle et al., 2010). In contrast, data for other gas species such as H_2O and CO_2 are lacking for many volcanic systems where proximal measurements are challenging, particularly in a monitoring capacity.

Unmanned Aerial Vehicles (UAVs) are now bridging the gap between direct and remote measurements by enabling proximal sampling from a safe and accessible distance. Recent developments in drone technology (in terms of both physical capability and user-accessibility) have been matched by a drive towards increasingly lightweight and compact sensor payloads, such that the resulting Unmanned Aerial Systems (UAS) are rapidly becoming 'go-to' solutions for a wide range of volcanological applications. UAS are driving the greatest advances in those fields requiring either proximal measurements in extreme environments or large areal coverage, including lava flow mapping, constructing topographic models and eruptive volume estimations (Turner et al., 2017; Moussallam et al., 2016; Nakano et al., 2014; Muller et al., 2017; Darmawan et al., 2018; Favelli et al., 2018), post-eruption visual observation (Koyama et al., 2013), thermal imaging (Di Stefano et al., 2017), aeromagnetic surveys (Kaneko et al., 2011; Hashimoto et al., 2014), DOAS traverses for SO_2 flux determination, and volcanic gas measurements and sampling (McGonigle et al., 2008; Shinohara, 2013; Xi et al., 2014; Pieri et al., 2013; Diaz et al., 2015; Mori et al., 2016; Di Stefano et al., 2017; Rüdiger et al., 2018; Stix et al., 2018).

Plume compositions measured by UAS 1–2 km from the vent following the 2014 phreatic eruption of Mt. Ontake demonstrated a dominantly hydrothermal degassing source (low SO_2/H_2S molar ratios, combined with SO_2 concentrations <1 ppm), and were critical to safe monitoring of the post-eruptive state of the volcano (Mori et al., 2016). At Turrialba volcano, Costa Rica, SO_2 concentrations measured by UAS in the dilute distal plume (up to 3 km from the vent, measuring 0.3–20 ppm SO_2) were used to derive estimates of SO_2 emission rates using an inverse Bayesian modelling approach incorporating meteorological wind fields (Xi et al., 2017). A recent comparison of SO_2 fluxes obtained by traditional ground-based

DOAS traverses to those from drone-mounted DOAS (DROAS) demonstrated the utility of UAS for this application, with the additional ability to constrain wind speeds at plume altitude based on passive drift speed of the UAS (Stix et al., 2018). Furthermore, comparison of CO_2/SO_2 molar ratios obtained by ground-based multi-GAS and simultaneously by a UAS-based gas sensor unit at Masaya, Nicaragua (Rudiger et al., 2018; Stix et al., 2018), showed that downwind measurements using UAS in dilute plumes yield robust correlations between gas species that are comparable to those derived from proximal ground-based measurements. However, molar ratios in distal plumes (<5 ppm maximum SO_2) can be characterised by larger standard deviations than proximal crater rim measurements (<38 ppm SO_2; Rudiger et al., 2018), highlighting that, although feasible, challenges still remain in acquiring high quality data from dilute plumes. This is particularly true for gas species such as CO_2, which have much higher background concentrations in ambient air (e.g., Aiuppa et al., 2009). Recently, Rudiger et al., (2018) demonstrate that UAS now enable the measurement of reactive halogen species in previously inaccessible downwind plume regions, and present proof-of-concept data that suggest an interesting potential relationship between Br_x/SO_2 and CO_2/SO_2 at Stromboli, Italy.

In-situ measurements of volcanic gas composition are particularly suited to a UAS-based approach as sampling young, high-temperature plumes minimises the effects of atmospheric interactions that dilute and chemically modify the gas composition, and thus reduce the fidelity of the signal. Here, we investigate short-timescale spatial and temporal variability in CO_2, H_2O, SO_2, H_2S, and HCl emissions within a very young plume at Volcán Villarrica, Chile. Villarrica is historically the most active volcano in Chile, and is one of only six volcanoes worldwide to host an open lava lake at its summit. It is a persistent emission source, and exhibited a notable compositional excursion in gas ratios prior to the last major eruption in March 2015 (Aiuppa et al., 2017b). The accessibility to the open summit vent, together with the permanent multi-GAS instrument located on the crater rim for data comparison, makes Villarrica an ideal natural laboratory for UAS field testing. Specifically, we present UAS-measured gas molar ratios in combination with SO_2 flux estimates derived from remote UV camera measurements, to quantify periodicities in gas composition and flux (on timescales of tens of seconds to minutes). We describe the development and deployment of two instrumented UAS: a customised Vulcan Black Widow multi-rotor UAV carrying a live-telemetered multi-GAS payload, designed specifically to withstand challenging environmental conditions during static hovers in the concentrated plume, and a modular

sensor attachment (Airgraph Aeris commercial prototype) to a DJI Phantom 3 Pro quadcopter offering agile mobility in the plume for large-scale SO_2 mapping.

The results presented in this study highlight previously unrecognised periodic degassing behaviour at Volcán Villarrica, and demonstrate further the validity of UAS for high-resolution studies and routine monitoring of volcanic emissions, more generally. Together with a suggested pre-flight checklist for UAV safe operation published as supplementary information, this work contributes a solid foundation on which to further advance the use of UAS for volcanic gas sensing, with future research focused on achieving long-range missions (>3 km) and coordinated multi-UAS experiments at strongly degassing but inaccessible volcanoes.

2. Geological Setting

Volcán Villarrica (2847 m AMSL) is a partially glaciated stratovolcano within the Southern Volcanic Zone (SVZ) of the Andes of Chile. The SVZ is a relatively carbon-poor volcanic arc segment compared to other arcs globally (Shinohara and Witter, 2005; Aiuppa et al., 2017a), with limited involvement of subducting slab-derived fluids in magma genesis (Jacques et al., 2013; Wehrmann et al., 2014). Villarrica's volcanic edifice hosts a persistently-degassing open lava lake at its summit, which is periodically perturbed by Strombolian explosions and transient lava fountaining (Calder et al., 2004; Palma et al., 2008). Erupted magma compositions range from basaltic to basaltic andesite (50–57 wt % SiO_2; Moreno et al., 1994; Witter et al., 2004; Hickey-Vargas et al., 2004), and include several mafic ignimbrites emplaced during Plinian eruptions during the Holocene (Parejas et al., 2010; Costantini et al., 2011). Historical eruptions, documented since 1558, have been predominantly characterised by mild/moderate explosive fountaining with occasional lava effusion. The surface of the lava lake fluctuates from <50 to >200 metres below the crater rim on monthly timescales, and indicates the top of the magma column that resides in the main conduit (Calder et al., 2004; Palma et al., 2008; Richardson et al., 2014; Moussallam et al., 2016). Variations in lava lake level are broadly correlated with both seismicity and degassing flux: periods when the lava level is high in the conduit are typically associated with more vigorous bubble bursting activity, higher SO_2 fluxes, and elevated RSAM seismic amplitude (Palma et al., 2008).

Villarrica is a persistent emission source within the SVZ, and has maintained an SO_2 flux on the order of a few hundred tonnes per day (t/day) during several campaign measurements since 2005 (Shinohara and Witter, 2005; Sawyer et al., 2011; Mather et al.,

2003; Moussallam et al., 2016), and by a permanent DOAS network since 2010 maintained by the Southern Andes Volcano Observatory (OVDAS). From January 2010 through May 2012, the lava lake surface was continuously visible and SO_2 emission rates averaged 926 t/day (OVDAS, *pers. comm*). Following subsidence of the lava lake out of view in June 2012, the emission rate reduced to an average of 386 t/day until February 2015 (OVDAS, *pers. comm*). Prior to the paroxysmal eruption of 3 March 2015, volcanic infrasound signals recorded a rapid increase in the level of the magma free surface from a stable level at >120 m below the crater rim to <70 m in the days prior to the eruption (Johnson et al., 2018). Following the eruption, the lake level remained high, maintaining an average SO_2 flux of 714 t/day until December 2017 when the magma column again withdrew out of sight (OVDAS, *pers. comm*).

A permanent, fully autonomous multi-GAS station installed on the eastern side of the summit crater detected a significant compositional excursion in molar gas ratios towards more CO_2-rich compositions immediately prior to the last major eruption in March 2015 (Aiuppa et al., 2017b). Although the instrument was destroyed during the intense lava fountaining activity of 3 March, a replacement station was re-installed in late November 2017, and acquires data during four 30-minute sampling windows each day. Previous campaign measurements using ground-based multi-GAS instruments at Villarrica (Shinohara and Witter, 2005, Aiuppa et al., 2017b, Moussallam et al., 2016) have not identified any clear periodic gas compositional variations associated with observed lava lake dynamics, but it remains unresolved whether this reflects the true degassing signature or is the result of homogenisation and dilution during plume transport to the crater rim.

3. Methods

3.1 Unmanned Aerial System (UAS) design

Volcanic gas sensing requires a vehicle that is robust and resilient in the field, resists acid gas corrosion, and has sufficient propulsion and mobility to remain stable in strong winds. In response to these criteria, together with the need for modular attachment of sensor packages, we developed a bespoke UAS based on a multi-rotor platform. The multi-rotor configuration was selected over a fixed-wing design for this field campaign due to the need to maintain a static hover at a single position in the plume, and to approach the vent in close proximity.

The vehicle was an octocopter in the X8 configuration based on a Vulcan 'Black Widow' frame with hub-to-hub diameter of 120 cm (Vulcan UAV, UK). Lift was provided by eight 16-inch propellers with a hub-to-hub dimension of 140 cm. The mass of the frame,

instrument payload, and batteries were 6.2 kg, 0.8 kg, and 3.5 kg respectively, resulting in a combined take-off weight of 10.5 kg. Maximum take-off weight is 16 kg. The vehicle used six 4250 mAh capacity batteries, each with a nominal voltage of 24 V (6S). When testing at an altitude of 250 m AMSL prior to summit ascent, the vehicle comfortably achieved a 13 minute flight duration with large capacity margins remaining in the battery. Given the performance degradation expected with the increased altitude (2847 m) and wind speed at the summit, flight durations were conservatively limited to 13 minutes or until the battery voltage dropped below 22 V, whichever occurred sooner.

The avionics comprised several commercially available products, selected for their reliability and long-range capabilities. The flight computer is a Pixhawk 2.1 auto-pilot (Hex Technology, Hong Kong) with associated GPS module. All flight critical electronics were housed in sealed enclosures to reduce exposure to acidic volcanic gases and prevent corrosion. For the flight computer, a small hole was required in the case to allow for pressure equalisation for the barometric altimeter, however the hole was sufficiently small to prevent significant airflow. Three separate radio-frequency links were used to communicate with the vehicle. The primary pilot control link used a transceiver set (Dragon Link, USA), operating on the 433 MHz frequency. An on-board video link used a transmitter and receiver set (ImmersionRC) on the 2.4 GHz frequency. The live video stream was made available to both the pilot and ground station via a first-person-view (FPV) headset and handheld screen, thus allowing the vehicle to be visually positioned in the dense plume. The third link provided a stream of live flight data using RFD868+ radio modems (RFDesign, Australia) operating on the 868 MHz frequency. Transmitted live data included information on the vehicle status, such as battery voltage and altitude, and real-time gas concentrations from the on-board multi-GAS sensor. The transmission of live sensor data to the ground-station was achieved by transcoding the digital Multi-GAS serial messages into the commonly used MAVLink protocol using a Teensy 3.6 microcontroller.

3.2 Multi-GAS

Concentrations of CO_2, SO_2, and H_2S (along with pressure, temperature and relative humidity) were measured at a 1 Hz sampling rate within the volcanic plume using a miniaturised multi-component gas analyser (multi-GAS; see Table S1, supplementary information, for detailed specifications of all components; Aiuppa et al., 2005, 2007, 2009; Shinohara et al., 2005), customised to be flown on a multi-rotor UAS (Section 3.1). The CO_2 spectrometer unit was wrapped in brass foil to shield the sensor board from radio frequency

interference from the UAS transmission system. H_2O concentrations were calculated from records of temperature and relative humidity measured on-board the UAS, using a time-average pressure of 724 ± 0.5 mbar. Air was sampled through a 1 µm particle filter exposed to ambient air, at pump rate of 1.0 L/min. The multi-GAS was calibrated with standard references gases at INGV Palermo two weeks prior to the field campaign, and again two weeks after. No significant sensor drift requiring data correction was identified. All sensor data was logged on-board, and also telemetered directly to the ground station where it could be visualised in real-time. Full specifications of the permanent ground-based multi-GAS station are given in Aiuppa et al., (2017).

Multi-GAS concentration timeseries were post-processed using Ratiocalc software (Tamburello, 2015). CO_2 concentrations were corrected internally for temperature (±0.2% full span per degree Celsius) and pressure (±0.15% per hPa). No pressure correction was applied to SO_2 or H_2S timeseries; however, applying the manufacturer compensation of 0.01 (SO_2) and 0.008 (H_2S) % signal per mbar to a subset of the data shows a +2.9% increase in SO_2 concentrations (Fig. S1, supplementary information; Kelly, 2017). This pressure effect translates to a maximum under-estimation of 3.5 ppm at 120 ppm SO_2, and <1 ppm under-estimation at <35 ppm SO_2. Importantly, however, barometric pressure varied by <2 mbar over the duration of the flight, so the temporal properties of the timeseries cannot be attributed to pressure fluctuations. Volcanogenic CO_2 was resolved from atmospheric background by subtracting the CO_2 concentration in ambient air (450 ± 5 ppmv; measured outside the plume where SO_2=0) from the raw CO_2 timeseries. No baseline drift correction was required for any gas species. H_2S concentrations were corrected for 13% cross-sensitivity to SO_2 ($H_2S_{corrected}$; Tamburello, 2015), where the magnitude of the cross-sensitivity was determined from laboratory tests using standard reference gases.

Molar ratios (CO_2/SO_2, H_2O/CO_2 and CO_2/H_2O) were derived from gas-gas scatterplots by calculating the gradient of the best-fit linear regression line through the data. Datapoints where SO_2 is present at <5 ppmv were excluded from the regression due to the greater error associated with very dilute plumes (e.g., Aiuppa et al., 2009); and >120 ppm due to the breakdown of the calibration curve above this concentration (the specific SO_2 sensor model used here is expected to exhibit a linear response in the 0–100 ppm ± 20% range). Uncertainties in derived molar gas ratios are ≥6.4% at >10 ppm SO_2 level and 12.5% at <10 ppm SO_2, based on the results of laboratory tests (Figures S2 and S3, supplementary information). Uncertainties on derived CO_2 and H_2O volatile fluxes are based on the

propagation of errors from both the molar gas ratios and the UV camera-derived SO_2 flux timeseries (see Section 3.6), assuming a conservative uncertainty on the molar ratio at ±12%.

3.3 Sensor response effects

During sampling and measurement, the sensors themselves act like filters and therefore the measured gas concentrations may be different from the true input signals, in particular if these undergo high frequency or rapid variations. The results presented here should therefore be looked at in conjunction with knowledge of the dynamic response of the specific sensors and system integration used. During tests it was found that these can be modelled using characteristic delays in series with either a first order or rate limited response where the delay can be considered to be the physical time it takes for the gas signal to reach the sensor from the inlet. To characterize the sensors, we performed controlled step tests at INGV Palermo with the Multi-GAS used in this study, during which the sensors were exposed to a range of known gas concentrations introduced 'instantaneously' at known times. We then modelled the sensor response using simulated signals, to determine the best-fit delay and dynamic parameters (Fig. 5a-d, supplementary information). For the current sensor configuration, it was found that the SO_2 electrochemical sensor can be characterized by a delay of 3 s together in conjunction with a first-order response with a time constant of 3.5 s. The CO_2 NDIR spectrometer can be best modelled with a rate-limited response of 35 ppm/s and a delay of 5 s.

The effect of the SO_2 sensor is therefore to act as a low pass filter with a corner frequency of 0.29 rad/s (0.045 Hz), reducing measurements varying at high frequencies when compared to the true values. It can also be seen that the effective non-linear rate limiting behaviour of the CO_2 NDIR will also reduce high frequency-varying measurements when compared to the true values. To demonstrate the effect of one of these sensors, we can consider the measured SO_2 relative to the true values time series from Flight V1 to be the true, raw gas concentrations and pass them through the first order model to derive the 'filtered' timeseries. The output signal was then processed using RatioCalc in the same way as our measured dataset (as described above) and we find that the measured SO_2 signal is delayed and attenuated in amplitude by 7–30% (8–22 ppm; depending on duration of exposure to the peak concentration) relative to the input signal (Fig. 5e-f, supplementary information). Whilst theoretically it is would be possible to retrieve additional amplitude and error information with regards to the original raw values using an inverse approach and with

significant post processing of the results, this is beyond the scope of this paper and is the subject of ongoing work.

Instead, the different gas timeseries were harmonised by applying a Savitzky-Golay lowpass least-squares filter to the SO_2 (13-point bandwidth, order 2) and H_2O (10-point bandwidth, order 2) timeseries, then determining the time offset required to maximise the correlation coefficient during linear regression with the unfiltered CO_2 timeseries (Fig. S5; Tamburello, 2015). The Savitsky-Golay filter was used specifically because it more effectively preserves peak height and width during noise reduction, which are usually attenuated by a moving average filter, however peak amplitudes can be degraded by ~5% during harmonisation. To further evaluate the error on the ratio resulting from differences in sensor response times (and thus the amplitude and width of peaks), the point-to-point regression-derived ratio was compared to that obtained by peak area integration, for each peak individually (Fig. S6, supplementary information; Shinohara et al., 2005). Close agreement is observed between the two methods, with the point-to-point regression typically yielding molar ratios ± 4 % of the ratio derived from integration (Fig. S6b).

3.4 Airgraph Aeris gas sensor unit

SO_2, H_2S, and HCl concentrations (along with pressure, temperature and relative humidity) were measured at a 1.25 Hz sampling rate within the volcanic plume using a commercial prototype Aeris gas analyser (Airgraph Instruments, Australia; Fig. 1e; see Table S1, supplementary information, for detailed specifications of all components) flown on a DJI Phantom 3 quadcopter UAV customised with a long-range transmission unit. The complete sensor package (including sensors, pump, tubing, outer casing and wireless telemetry unit) has a mass of ~300 g and has been designed specifically to integrate with the Phantom series by clipping to the struts beneath the camera gimbal as a removable modular unit. The Aeris is controlled through an external laptop via a USB connection, which is then disconnected prior to takeoff once the Aeris has begun logging. All data is logged on-board, and downloaded in the field by reconnection of the unit to the external laptop immediately after landing. The raw Aeris data were analysed in the same manner as described above for multi-GAS data, using Ratiocalc software (Tamburello, 2015).

3.5 Field deployment of UAS

We deployed the two gas analyser-equipped UAS in the plume of Volcán Villarrica on 19 and 20 March 2018, as part of a longer field campaign at the same volcano spanning 13–27

March 2018 (Table S2, supplementary information). The wind speed on all other days of the field campaign were too high at the summit for additional flights. Full permissions for aerial work were obtained from the Chilean Dirección General de Aeronáutica Civil (DGAC). Permissions were granted for line-of-sight (LOS) operations within a specified area around the summit region, with a maximum flight altitude of 400 ft AGL. A copy of the pre-flight checklist is included in the Supporting Information (Text S1, supplementary information). This checklist was completed before every flight, and covers actions related to planning (e.g, defining a flight plan and objectives), ensuring the vehicle is flightworthy (e.g., battery and GPS checks), and recording relevant flight data to inform future operations (e.g., duration and battery usage). The checklist is not designed to be exhaustive and does not replace or ensure the competence of the operators, but rather mitigates against the risk of human error when operating in extreme environments. Although the checklist included in the Supporting Information (Text S1) is aimed at the UAS used in this study, many of the checks performed are applicable and transferable to UAS operations more generally.

The weather on both measurement days was clear, with very low humidity and wind speeds <10 m s^{-1} at summit altitude. The atmospheric conditions were thus extremely favourable for gas measurements and within the wind tolerance envelope for UAV flights. The UAS were launched from a plateau just inside the crater rim on the northern side of the summit, at an altitude of 2850 m AMSL (Fig. 1). Flight durations for the Vulcan multi-rotor ranged from 9 to 12 minutes. Average power consumption during flight was ~1880 W. The UAS were operated within visual line of sight (VLOS) at all times, and due to the proximity of the plume to the take-off location the vehicle was manually piloted in the LOITER mode (GPS-assisted positioning). This mode provides position and orientation stability to automatically resist disturbances caused by wind or the turbulent plume. The multi-GAS and Aeris instruments were set to start logging up to 10 minutes prior to takeoff to allow sufficient time for the sensors to equilibrate and for the IR spectrometer to reach operating temperature (the warm-up time is 2 minutes, but stability continues to improve up to 30 mins). Flight paths were specific to each UAS, and were chosen based on the scientific objective of each flight.

Flight Objective 1 – Plume mapping: Gas concentrations in volcanic plumes are spatially heterogeneous due to a combination of both primary variability in degassing and interaction/entrainment with atmospheric air (Tamburello et al., 2012, 2013; Pering et al., 2014 and others). Plume identification was complicated further during our campaign because the plume was entirely non-condensing in the low humidity, and the extremely low level of

the lava in the conduit meant the degassing source was not directly visible. To determine the most concentrated region of the plume for subsequent static hover flights, the Phantom-mounted Aeris sensor was flown in traverses across the crater, perpendicular to the wind direction, at approximately constant altitude to map out the typical cross-sectional structure of the volcanic plume within the Villarrica crater.

Flight Objective 2 – Static hover: Temporal variations in volcanic gas flux and/or composition can provide insight into the nature of the degassing source, especially if these changes can be correlated with other observational variables. To measure a degassing timeseries, the Vulcan multi-rotor was deployed to perform a static hover in the most concentrated part of the plume. The initial UAS positioning was chosen using the region of highest gas concentration within Aeris plume maps, and was further refined during flight in response to close monitoring of the live telemetry feed to maximise real-time measured concentrations.

3.6 PiCam UV camera

The PiCam UV camera system uses two co-aligned Raspberry pi cameras with horizontal field of view 23.1°, with optical filters (Edmund Optics Ltd.) centred at 310 (SO_2 absorption) and 330 nm (no SO_2 absorption; Wilkes et al., 2016, 2017). Images were taken at a frame rate of 0.125 Hz, using shutter speeds of 1100/1400 ms and 100 ms for the 310 and 330 nm filters, respectively. The UV camera was located directly north of the summit vent on 26/03/2018 (39˚22'38.64" S, 71˚56'46.99" W), ~5.1 km from the plume and perpendicular to the plume transport direction. Calibration was performed using three quartz cells containing known column amounts of SO_2 (0, 304 ± 31 and 1257 ± 58 ppm·m), and re-calibrated every 90 mins or whenever background conditions changed, whichever was sooner. The gas cell column amounts were measured independently using DOAS. Taking the largest cell uncertainty, we ascribe a ±10% uncertainty to the calibration cell column amounts, based on 10 repeat measurements of each cell. Clear sky images for vignette correction and dark images were also collected at these times.

Atmospheric conditions throughout acquisition were optimal for spectroscopic measurements, with a near-transparent, non-condensed plume with clear edge definition at all times and a cloud-free homogenous background. Errors resulting from light dilution (i.e., scattering of photons between the plume and the instrument within the field of view) are therefore dominated by the viewing distance and absolute SO_2 integrated column amounts, and are likely towards the lower end of the 20–80% range of uncertainty demonstrated by

Campion et al., (2015). Absolute scattering uncertainties could not be determined following the method of Campion et al. (2015), due to the presence of snow on the slopes. Furthermore, uncertainty arising from variations in the viewing distance cannot be fully quantified without exact independent knowledge of the plume position; however, we minimise this uncertainty by taking an integration line as close as possible to the edifice, which is of known distance at 5100 m. We approximate this error using a value of ±500 m (towards the upper end of potential variations given mitigations already in place), which translates to a ±10% error in flux estimates.

Image sequences were post-processed using custom Python 3 software (including image alignment, vignette and dark image correction; Wilkes et al., 2016, 2017), before creation of absorption images (see Fig. 5 for example). Plume speeds were calculated using the optical flow method (Peters et al., 2015a) over cross-correlation, as motion estimation algorithms have been shown to yield more robust velocity estimates during benchmarking simulations (Peters et al., 2015b), and to enable direct comparison with previous UV camera data from Villarrica (Peters et al., 2015; Moussallam et al., 2016). Calculated plume speeds range from 0.01 to 30 m s^{-1} with optical registration errors of 1.2% to 77% (however, 91% of the errors are <10%, with a median error of 3.8%). The magnitude and variance of the errors are generally lower for higher plume speeds (Fig. S7, supplementary information). To obtain a timeseries of SO_2 flux (kg s^{-1}), plume speeds are multiplied by the corresponding integrated SO_2 column amounts. For full details on protocols for UV camera measurement and post-processing see Kantzas et al., (2010) and McGonigle et al., (2017). Combining the stated uncertainties associated with calibration, light scattering, viewing distance and plume speed determination, we calculate a root mean square (RMS) error on the derived SO_2 fluxes of 12–41%.

3.7 Timeseries analysis

Volcanic systems, and open-vent volcanoes in particular, exhibit strongly periodic degassing behaviour on a variety of timescales (e.g., Tamburello et al., 2012, 2013; Nicholson et al., 2013; Pering et al., 2014a, b; Flower and Carn, 2015). The signals of multiple, superposed cycles within a timeseries can be deconvolved by spectral analytical approaches, such as Fast Fourier Transform (FFT) and Continuous Wavelet Transform (CWT), to reveal the frequency, and relative dominance, of underlying periodic components (e.g., Percival and Walden, 1993, 2006; Torrence and Compo, 1998). In this study, the cyclical character within timeseries of gas flux (UV camera) and concentration (multi-GAS) were quantified using

both CWT and FFT methods. Prior to analysis, the timeseries were smoothed using a Savitzky-Golay filter (which minimises the least-squares error in polynomial fitting) and normalised to a zero-mean distribution. An additional requirement of FFT is that the timeseries are truncated to a length of 2^n samples (for integer n).

For FFT, Thompson's Multitaper Method (MTM) was implemented as it provides the most robust estimate of the power spectral density (PSD) at each frequency when there is no prior assumption of the signal generating source (Thomson, 1982). Statistical stationarity, required over the complete data window for MTM analysis, may not be appropriate for many geophysical systems known to exhibit temporal evolution in cyclic behaviour; non-stationary yields broad undefined peaks in frequency spectra that are difficult to interpret, or masks the periodic component entirely. Moving-window FFT, where a series of PSD estimates are calculated using a shorter moving window of $2^{(n-1)}$, has been applied to volcanological datasets to account for temporal heterogeneity in the frequency-domain (Odbert and Wadge, 2009; Nicholson et al., 2013; Lamb et al., 2014); however, this approach still requires the assumption of stationarity over the length of the moving window.

Wavelet analysis, here in the form of the continuous wavelet transform (CWT), offers additional degrees of freedom, such that not only can the requirement for stationarity be relaxed but the temporal persistence of cyclic components can be investigated in detail (e.g., Torrence and Compo, 1998; Percival and Walden, 2006). In comparison to FFT, which compares the signal to sine waves of different frequencies, wavelet transform compares the signal to scaled (dilation in the frequency domain) and shifted (translation in the time domain) versions of a "mother wavelet", for which the transform power at each time-frequency position can be visualised as a colour-scaled scalogram. Whilst sine waves are smooth and infinitely-repeating, wavelets are irregularly shaped and decay over a finite length; wavelets are therefore suited to analysing unstable periodic phenomena or resolving discontinuities with high temporal localisation. Here, we compare our SO_2 flux and concentration timeseries to the *Morlet* mother wavelet (which resembles a sine wave that decays with time away from its centre) as it possesses many similarities to naturally occurring oscillations observed within the geosciences (Morlet, 1982; Torrence and Compo, 1998; Odbert and Wadge, 2009; Pering et al., 2014; Odbert et al., 2014). Edge effects resulting from the discrete nature of the timeseries may manifest as artificially high/low transform values in the CWT. The region of the CWT scalogram potentially affected by these edge effects is defined by the wavelet-specific cone-of-influence (COI).

4. Results

4.1 Visual observations

Throughout our measurement campaign the plume transport direction was towards the E to NE, consistent with the prevailing wind direction for the region and season, and was persistently fumigating the permanent multi-GAS station on the crater rim. The lava lake level was extremely low in the conduit, such that the free surface was not visible directly from the crater rim. Aerial observations using a UAV-mounted nadir camera showed the lava lake to comprise only a few pixels of the image (Fig. 1c), confirming that the top of the magma column was residing several hundred metres below the summit elevation. We observed near-continuous passive degassing during a total of 18 hours (cumulative) spent at the summit, punctuated by active degassing pulses associated with audible gas exhalations (bubble bursts) from the lava lake below. Each audible exhalation lasted between 1 and 5 seconds (with the longer events comprising multiple discrete bursts) and was followed approximately 10 seconds later by the appearance of a buoyantly rising gas plume at the top of the conduit. The plume rose vertically above the vent until approximately level with crater rim, after which it began to interact with atmospheric winds and move laterally and more turbulently.

Active degassing, in the form of discrete gas exhalations, was clearly observed during our instrumented UAS flights and manifested in several quantifiable parameters in addition to the live telemetered gas concentration. The arrival of each pulse of gas at the UAS was immediately accompanied by an abrupt increase in both hover turbulence and ambient temperature.

4.2 Compositional mapping through a plume cross-section

The spatial distributions of SO_2, H_2S and HCl within a 2D cross-section perpendicular to the plume transport direction were acquired during two flights on 20/03/18 (P3, P4; Table S2) and a further flight on 21/03/18 (P5). Sampling locations from the two flights on 20/03/18 are displayed as a GoogleEarth overlay according to the GPS position of the UAS at the time of measurement, and coloured according to measured gas concentrations (Fig. 2). All flights were approximately 15 minutes in duration, and therefore the maps shown in Figure 2 combine measurements acquired over ~30 minutes. Although time-averaging in this way precludes identification of short-term temporal variations, the overall spatial distribution of degassing sources is likely to have remained relatively constant during the time interval of acquisition. The concentrations of all gas species are clearly elevated within a region in the S-

SSE of the crater area, suggesting that this is the densest part of the plume and thus providing the target for the static hover UAS missions. H_2S concentrations were below the 13% cross-sensitivity to SO_2, and are therefore not shown on Figure 2. The temporal superposition of concentrated gas pulses on dilute passive degassing may explain why some locations with overlapping transects have such contrasting concentrations.

4.3 Molar gas ratios

Elevated concentrations of CO_2, SO_2, and H_2O relative to atmospheric background were encountered throughout UAS hover flights (V1 and V2; Table S2; Fig. 3). H_2S concentrations were below the 13% cross-sensitivity to SO_2 with the exception of a single peak (>100 ppmv SO_2) where the $SO_2/H_2S_{corrected}$ ratio was 0.08, which we take to represent the lower limit on this molar ratio. SO_2 concentrations span two orders of magnitude from $<10^{-1}$ to $>10^2$ ppmv. Peak concentrations during active degassing pulses occasionally exceeded the calibrated range of the electrochemical sensor, resulting in truncation of peak concentrations; saturated values >120 ppmv were excluded from subsequent ratio calculations, but represent less than 5% of the data. Measured CO_2 concentrations reached up to 987 ppmv, indicating volcanogenic contributions of $\leq$ 450 ppmv after subtracting ambient atmospheric background.

Temporal variations in CO_2, SO_2, and H_2O yield good to very good statistical correlations between species (Fig. 4; Table S3, supplementary information), and thus well constrained molar gas ratios. We derived CO_2/SO_2 ratios of 1.48 ± 0.06 and 1.68 ± 0.03, H_2O/SO_2 ratios of 67 ± 1.85 and 75 ± 1.74, and H_2O/CO_2 ratios of 44 ± 0.9 and 51 ± 1.49 (Table S3, supplementary information; the quoted uncertainty is the 95% confidence interval of the regression), each for flights V1 and V2 respectively. We find that variability in molar gas ratios is related to plume density, such that CO_2/SO_2 ratios are both elevated and more variable in dilute plumes (<20 ppmv SO_2, where SO_2 is taken as the 'plume marker' due to the negligible content in ambient air). The effect of measurement uncertainty on CO_2/SO_2 is amplified as the denominator approaches zero; however, we also acknowledge that diffuse CO_2-rich degassing from the crater rim may contribute to more variable molar ratios at low SO_2 (Stix et al., 2018). In dense plume conditions (>20 ppmv SO_2), the CO_2/SO_2 ratio converges and stabilises at lower values approaching 1.69 ± 0.34 (Fig. S8, supplementary information).

H_2O is well correlated with both SO_2 and CO_2, despite being calculated entirely independently of both variables (e.g., H_2O/SO_2 = 67 and 75 for flight V1 and V2

respectively; R^2 between 0.94 and 0.96). The strength of this correlation reflects the extremely low humidity conditions under which these data were acquired (Rh <10% at summit altitude). The plume was non-condensing and almost transparent throughout the measurement period, thus producing an exceptionally smooth H_2O trace with a high signal-to-noise ratio.

4.4 SO_2 flux

A timeseries of SO_2 emission rates was derived from 3 hrs 45 mins of UV camera acquisition on 26/03/2018 (n=1430; Fig. 5). SO_2 flux ranged from 0 to 12.4 kg s^{-1} (17 to 1071 t/day) during the measurement period, with a median flux of 1.64 ± 0.2 kg s^{-1} (142 ± 17 t/day; the quoted uncertainty represents the RMS error at ± 12%, please see the methods for a discussion of the main sources of uncertainty). Median plume speeds calculated for each acquisition period individually are 4.33 ± 0.2 m s^{-1} (section 1b), and 7.12 ± 0.3 m s^{-1} (section 2), yielding median fluxes of 1.54 ± 0.2 kg s^{-1} (section 1b) and 1.90 ± 0.2 kg s^{-1} (section 2), respectively. Note that the PiCam was re-calibrated between sections 1 and 2.

Periodic degassing behaviour was noted in the field, and is clearly visible in the absorbance images and flux timeseries. An animated GIF of absorbance images from first half of section 2 provides a visual representation of the pulsatory behaviour (Video S1, supplementary information). An individual SO_2 pulse is magnified in figure 5b, together with pseudocolour images of SO_2 integrated column amounts corresponding to specific annotated positions on the flux timeseries (Figs. 5c–g). The SO_2 flux is positively correlated with the calculated plume speed, such that peaks in SO_2 flux reflect discrete, buoyant gas-rich exhalations.

5. Discussion

5.1 Volatile fluxes

The molar plume compositions are comparable between the two flights: 96.4 mol% (H_2O), 2.13 mol% (CO_2), and 1.44 mol% (SO_2) for flight V1 and 96.6 mol% (H_2O), 2.17 mol% (CO_2), and 1.29 mol% (SO_2) for flight V2. Combining in-plume molar gas ratios (converted to mass ratios) with the time-averaged SO_2 flux derived from remote UV camera measurements, we estimate the mass flux of CO_2 and H_2O (Table S4, supplementary information). For a median SO_2 flux of 1.64 ± 0.2 kg/s (Fig. 5) and the molar ratios shown in Table S3, we calculate emission rates of 1.68 ± 0.3 and 1.89 ± 0.3 kg/s (144 ± 24 and 163 ±

28 t/day) for CO_2, and 30.6 ± 5.2 and 34.5 ± 5.9 (2670 ± 453 and 2981 ± 506 t/day) for H_2O, each for flights V1 and V2 respectively. Calculated plume compositions from this study are almost identical to those determined previously by Shinohara and Witter (2005) – 95 mol% H_2O, 2.0 mol% CO_2, 2.1 mol% SO_2, <0.01 mol% H_2S and 0.63 mol% HCl – thus highlighting a remarkable stability in the composition of the gas phase outgassed during 'background' activity at Villarrica over decadal timescales. The low molar proportion and flux of CO_2 (for example, compared to the 2850–3900 t/day CO_2 emitted at Etna, Italy; Santoro et al., 2017) are consistent with the overall carbon-poor character of the SVZ.

The SO_2 flux during this campaign (142 ± 17 t/day) is within the range of previous flux measurements at Villarrica, which range from 40 to >1000 t/day (Shinohara and Witter, Mather et al. 2003, Palma et al., 2008; Moussallam et al., 2016). On timescales of weeks to months the SO_2 flux appears to be strongly coupled to the lava lake dynamics, such that periods of elevated seismicity where the lava lake surface is at a high level in the conduit are associated with stronger SO_2 degassing (Palma et al., 2008). Campaign measurements between 2000 and 2006 show that emissions during low level 'background' activity are characterised by a relatively constant flux on the order of a few hundred tonnes per day SO_2 (150–500 t/day), with rare transient excursions to higher values (up to ~1000 t/day; e.g., January 2005; Palma et al., 2008). Most recently, Moussallam et al., (2016) reported SO_2 emission rates between 40 and 260 t/day from high-resolution UV camera images (during 1 hr of acquisition on 9 February 2016), with an average value of 160 t/day. At the time of measurements in February 2016, the lava lake level was low in the conduit (~140 m below the crater rim), with exposed surface area of ~700 m^2 (Moussallam et al., 2016). The state of the lava lake was therefore comparable to that observed during the present study, although we estimate the lava lake level in March 2018 to have been deeper (>200 m below the crater rim), and characteristic of 'background' activity.

5.2 Comparison of UAS- and ground-based multi-GAS measurements

The second UAS flight (V2) was timed to coincide with the 30-minute acquisition window (18:05–18:35 UTC) of the ground-based semi-autonomous multi-GAS station located on the eastern side of the crater rim. Using SO_2 as the plume marker due to the negligible concentration in ambient air, Figure 6 shows that the concentrations measured by the UAS are an order of magnitude higher than those detected by the crater rim station, despite being located only ~100 m apart. SO_2 concentrations reaching the crater rim multi-GAS did not exceed 10 ppm on either of the measurement days, yet concentrations in excess of 100 ppm

were routinely detected by the UAS-multi-GAS during gas pulses (Fig. 6a). When displayed on different y-axis scales to expand the detail within the crater rim multi-GAS timeseries, we observe little similarity between the two concentration traces (Fig. 9b). This result is not unexpected, as we clearly observed in the field that as the plume exited the conduit it very quickly became dispersed by turbulent wind eddies within the crater region. This turbulence would quite effectively have homogenised the plume over the 10–15 seconds transport time required to travel 100 m lateral distance assuming plume speeds of ~5 m/s (based on the median plume speed derived by applying an optical flow algorithm to successive UV camera images; Section 3.6).

Nevertheless, considering daily average molar ratios (which for the crater rim multi-GAS represent the average ratio measured over 4 x 30 minute intervals each day) we observe good agreement between the UAS-based and ground-based systems (Fig. 7). Since installation of the crater rim multi-GAS station in early December 2017, CO_2/SO_2 molar ratios spanning a range from <1 to 15 have been reported. Elevated (but highly variable) CO_2/SO_2 ratios > 4 (average: 4.51 ± 2.3 [1σ]) were measured during the first section of the timeseries from 5–16 December 2017. After 16 December, ratios reduced abruptly and stabilised to values not exceeding 4. Over the period from 16 December to 25 March 2018, the average CO_2/SO_2 ratio was 2.46 ± 0.9 [1σ]. The more CO_2-rich gas compositions in early December occurred during a period of heightened activity, where the lava lake level was very high (Fig., 7b), strong incandescence was recorded (Fig. S9, supplementary information) and persistent MODIS satellite thermal anomalies were detected (MIROVA). During this period, vigorous bubble bursting and lava fountaining was observed from the crater rim and detected by the infrasound monitoring array, and RSAM seismicity was elevated (OVDAS Reporte Especial de Actividad Volcanica, 05 December 2017 09:50). The alert level at Villarrica was raised to yellow (from green) between 4 and 31 December. The marked decrease in the CO_2/SO_2 ratio in mid-December occurred coincident with an abrupt depression of the lava level that resulted in the complete disappearance of the lava lake surface from view (Fig. 7b) and the initiation of a hiatus in detectable thermal anomalies or incandescence (Fig. S9, supplementary information). These observations are entirely consistent with previous studies at Villarrica, which have demonstrated not only a strong positive correlation between degassing and RSAM/lava level (Palma et al., 2008), but also distinct changes in gas composition towards more CO_2-rich compositions during periods of heightened activity (Aiuppa et al., 2017b).

During the measurement campaign for this study, the CO_2/SO_2 ratio was particularly low and varied between 0.8 and 2.1, with an average of 1.5 (over four datapoints from 17 to 25 March 2018; Fig. 7). These values show close correspondence with the molar CO_2/SO_2 ratios of 1.48 ± 0.02 and 1.68 ± 0.03 obtained by the UAS-multi-GAS (flight V1 and V2, respectively). Unfortunately, it was not possible to compare H_2O/SO_2 or H_2O/CO_2 ratios as H_2O can only be measured in dense plume conditions (due to the high background concentration in ambient air) and is therefore rarely resolvable at the ground-based station. The low CO_2/SO_2 (<2) molar gas ratios suggest that during background low level activity degassing (both active and passive) is being driven by gas bubbles that have remained coupled to the magma until shallow pressures in the range 0.1–5 MPa (assuming closed system degassing from 200 to 0.1 MPa; Aiuppa et al., 2017b). In other words, the bubbles being actively outgassed at the surface have not separated from the magma during convective flow within the conduit, or at least not until near-surface conditions (Witter et al., 2004; Moussallam et al., 2016; Aiuppa et al., 2017). This low pressure degassing contrasts with the situation during elevated activity, where the CO_2-rich gas compositions suggest much deeper gas-melt equilibration, and thus more deeply-sourced volatiles (Aiuppa et al., 2006; 2010; 2017).

A single large bubble burst at the beginning of flight V1 (shown by the red symbols; Fig. 4a–c) is characterised by significantly higher CO_2/SO_2 (and slightly reduced H_2O/SO_2) compared to the tightly constrained bulk trend. The CO_2/SO_2 ratio of 2.42 calculated for this individual peak by regression (or 2.75 by integration) suggests gas-melt equilibration under slightly higher pressures than the rest of the bubble population, towards the upper end of the 0.1–5 MPa range (Aiuppa et al., 2017b).

5.3 Periodic timescales

The results obtained by applying wavelet analysis (continuous wavelet transform, CWT) and fast fourier transform (FFT) to UAS-based SO_2 concentrations are mutually consistent, and together indicate that the timeseries is composed of one or more periodic components superimposed on background noise (Fig. 8). MTM power spectra for the two static hover flights (flights V1 and V2) indicate a strong shared frequency component at 0.023 Hz, which corresponds to a cycle period of ~44 seconds (Fig. 8c, d). Flight V1 contains a second, more dominant, cycle at 0.004 Hz, or ~250 seconds. However, this component reflects the low concentration interval in the middle of the acquisition period, which imposes a symmetry to the timeseries that manifests as a cycle with wavelength equal to half the window length.

With only two cycles within the complete dataset we cannot determine if this low-frequency cycle is a true feature or simply an artefact of the data structure, and it will therefore not be considered further. Importantly, the broad spectral peaks suggest some degree of non-stationarity in the dominant frequency, with variability in the frequency domain that cannot be resolved by the fixed window length of FFT.

The CWT, expressed in the form of a scalogram, provides additional constraint on the time-frequency behaviour (Fig. 8a, b; note that the colour-scale corresponds to different ranges of transform magnitude for each flight). For flight V2, the strongest correlation with the wavelet (i.e., the region of highest wavelet coefficients) is observed in the frequency range 23–28 mHz, equivalent to cycles 36–43 s in duration. Although this band of high coefficients is present throughout the timeseries (with time increasing left to right), the absolute frequency does not remain constant. The dominant frequency migrates from 35 mHz (29 s period) at 0–40 s to 20 mHz (49 s period) at 168–250 s. At 250 s, the dominant frequent returns abruptly to 35 mHz, and remains near this value for the remainder of the timeseries. The frequency glide reflects a progressive lengthening of the cycle period with time, and, together with the abrupt discontinuity at 250 s, confirms non-stationarity within the timeseries. Similarly, flight V1 also shows high transform power in the range 25–31 mHz (32–40 s period) at the beginning and end of the timeseries. However, the periodicity breaks down in the centre of the timeseries, and instead becomes dominated by a low frequency component at ~4 mHz (~250 s; see discussion above). The CWT scalograms agree well with the results from static PSD spectra in terms of absolute cycle frequency, whilst providing additional information related to the temporal persistence of each cycle.

There are several processes that could generate the observed periodic variation in SO_2 concentration, including both primary (i.e., degassing dynamics) and secondary (e.g., atmospheric effects during transport from emission to the point of measurement) processes (Boichu et al., 2010). Transport effects within the crater itself include (a) local variability in wind speed, direction or turbulence, which would modulate the degree of atmospheric entrainment and thus plume dilution, or (b) turbulent diffusion (i.e., generation of eddies by convection) and progressive large-scale organisation of turbulence within the rising volcanic gas plume. However, the onset of each peak in gas concentration (as observed in the live telemetry data) was preceded by an audible bubble burst ~10 seconds prior to the emergence of a visible gas pulse appearing at the top of the conduit (vertical red lines on Fig. 3 represent the timing of recorded bubble bursts but is not a complete dataset) and an increase in thermal turbulence experienced by the UAS. Similar audible exhalations, followed by visible gas

pulses, occurred regularly throughout the observation time spent at the summit region on timescales of tens of seconds to minutes (although repose times were not recorded explicitly). These observations suggest that the peaks in concentration, and thus the periodicity, are directly linked to active degassing dynamics, in the form of discrete bubble bursts at the surface of the lava lake.

The identification of distinct, and relatively persistent, short-term cycles (30–50 s) in the degassing timeseries stands in apparent contrast to previous studies where no periodic behaviour was observed (Moussallam et al., 2016). These authors interpret the lack of structure in the gas signal to reflect turbulent mixing and homogenisation between ascending, buoyant gas-rich magma and descending, dense, degassed magma in the conduit (Moussallam et al., 2016). We propose that the contrasting behaviours observed may reflect a difference in the outgassing regime between the two field campaigns. Although during the present study the surface of the lava lake could not be observed directly, the audible exhalations implied a small number of large bubble bursts (1–2 per minute). However, if many smaller bubbles were bursting more frequently (similar to the 'seething magma' described by Palma et al., 2008) then one might expect the individual signature of each exhalation to be smaller in magnitude and superposed, thus producing an apparently structureless timeseries. We also note that whilst the UAS-based SO_2 concentrations measured during flight V2 exhibit periodic behaviour on timescales ~36–43 s, data acquired simultaneously by the ground-based multi-GAS on the crater rim show no such periodicity on any timescale (Fig. 6b). Plume dilution and turbulent mixing in the atmosphere, even within the crater region, thus appear to effectively homogenise any short-term variability.

The SO_2 flux timeseries derived from the remote UV camera images also displays strong periodic characteristics, but on significantly longer time-scales than observed in the gas concentrations within the young plume. The early section of section 2 (Fig. 9a) contains high transform power in the CWT scalogram centred on a frequency of 2.9 mHz (345 s/5.75 min period). With time, this cycle frequency gradually decreases to reach ~1.4 mHz (714 s/11.9 min period) where it once again stabilises in the final third of the timeseries. Although each gas pulse visible in the absorption images appears to have an impulsive rise component to its motion (Video S1, supplementary information) suggesting a buoyant primary exhalation, we cannot exclude the possibility that this longer period cycle reflects large-scale organisation of turbulence as the plume exits the crater and interacts with the atmosphere (Boichu et al., 2010). It is encouraging to see that even after pausing the acquisition, re-calibrating, and restarting the UV camera (Fig. 9b), section 3 of the SO_2 timeseries contains

the same low frequency component (~700 s period) identified in the latter part of section 2, and thus transitions almost seamlessly from the previous scalogram. Abrupt increases in SO_2 flux introduce sharp discontinuities into section 3 (most striking of which occurs at 0.35 hrs). These discontinuities are clearly manifest in the scalogram as transient high transform values across all scales.

6. Summary and conclusions

In this study, we demonstrate the efficacy of UAS-based gas measurements for investigating short-timescale variability in volcanic outgassing and plume transport processes, and for the derivation of well-constrained CO_2 and H_2O fluxes, which necessitate high plume to background concentrations. To maximise the efficiency of field deployment, we find that mapping the plume with smaller, lighter UAS and then using these data to locate the static hover (refined further by live data telemetry) provides an effective operational approach that ensures rapid positioning within the region of maximum gas concentrations. Our data show that SO_2 concentrations in the young proximal plume at Volcán Villarrica, Chile, exhibit periodic variations that are well-correlated with other gas species. Derived molar gas ratios (CO_2/SO_2 = 1.48–1.68, H_2O/SO_2 = 67–75 and H_2O/CO_2 = 45–51) are well-constrained with high statistical confidence. By combining in-plume molar gas ratios with the SO_2 flux (142 ± 17 t/day) from UV camera images, we derive CO_2 and H_2O fluxes of ~150 t/day and ~2850 t/day, respectively, consistent with the overall carbon-poor nature of magmas from the Southern Volcanic Zone of the Andes (Shinohara and Witter, 2005; Aiuppa et al., 2017a).

Periodic variations are clearly evident in the gas concentration timeseries obtained during static hover flights. Cycle periods vary between 30 to 50 s (with the strongest periodicity manifest at 36–43 s), with marked non-stationarity over the duration of the timeseries, based on both wavelet and fast fourier transform analyses of the frequency content of the measured signal. Peaks in gas concentration were preceded by audible gas exhalations, thus suggesting that the periodicity reflects a primary degassing process (i.e., individual bubble bursts), rather than atmospheric effects during plume transport. Active degassing through discrete gas exhalations therefore provides an important contribution to outgassing at Villarrica that modulates gas flux over timescales of tens of seconds to minutes. UV camera-derived SO_2 fluxes immediately above the summit crater are characterised by longer timescale periodicities (5–12 mins), which likely reflect superposition of both primary degassing and large-scale organisation of turbulence during the early phase of plume transport.

Simultaneous acquisitions by the UAS and a ground-based multi-GAS located on the crater rim highlighted that considerable plume dilution and homogenisation occurs during transport within the crater, over horizontal length scales of only ~100 m. UAS-based SO_2 concentrations (<120 ppm) are generally an order of magnitude greater than measured at the crater rim (<10 ppm), and exhibit much more regular, short-timescale variability that can be correlated with discrete outgassing events. Despite this, time-averaged molar gas ratios obtained by the two multi-GAS systems are in good agreement, and are consistent with a long-term decline in CO_2/SO_2 following elevated levels of activity (and more CO_2-rich gas compositions) in December 2017. The present low CO_2/SO_2 ratio <2 implies low pressure degassing in equilibrium with the shallow magma reservoir, and is representative of 'background' activity at Villarrica (Aiuppa et al., 2017b). We therefore highlight the potential for UAS-based measurements to be applied in complement to ground-based gas monitoring at Villarrica, particularly when the lava lake is very low in the conduit and the crater rim station is typically sampling only a very dilute or aged plume.

Acknowledgements

We are deeply grateful to both Richard and Coco of Sierra Nevada for their expert guiding during our multiple ascents of Villarrica, and their patience during many hours at the summit. We thank OVDAS for their collaboration and for liasing with CONAF for access permissions on our behalf, and Dr Ángela Hernández (Centro de Investigación en Ecosistemas de la Patagonia) for assistance in obtaining flight permissions from the DGAC plus her support, along with Giovanni Denari (CIEP) and Alejandro Miranda (Universidad de la Frontera) during the initial ascent of the volcano. This work was directly funded by a Leverhulme Early Career Fellowship to EJL, and an EPSRC postgraduate studentship to EM. TR and KW were supported by EPSRC through the CASCADE Programme Grant (EP/R009953/1). TDP acknowledges the support of the Royal Society (RG170226). IMW was supported by NERC through the Centre for the Observation and Modelling of Earthquakes, Volcanoes and Tectonics (COMET NE/J01978X/1). This research was supported through the Alfred P. Sloan Foundation's support of the Deep Carbon Observatory Deep Earth Carbon Degassing program (DECADE). We also thank Airgraph for the opportunity to be involved in the ongoing collaborative development and field testing of the Aeris. Raw data are available in the online supplementary information.

References

Aiuppa, A., Bertagnini, A., Métrich, N., Moretti, R., Di Muro, A., Liuzzo, M., Tamburello, G., 2010. A model of degassing for Stromboli volcano. Earth and Planetary Science Letters 295, 195–204. https://doi.org/10.1016/j.epsl.2010.03.040

Aiuppa, A., Federico, C., Giudice, G., Giuffrida, G., Guida, R., Gurrieri, S., Liuzzo, M., Moretti, R., Papale, P., 2009. The 2007 eruption of Stromboli volcano: Insights from real-time measurement of the volcanic gas plume CO_2/SO_2 ratio. Journal of Volcanology and Geothermal Research, The 2007 Eruption of Stromboli 182, 221–230. https://doi.org/10.1016/j.jvolgeores.2008.09.013

Aiuppa, A., Fischer, T.P., Plank, T., Robidoux, P., Di Napoli, R., 2017. Along-arc, inter-arc and arc-to-arc variations in volcanic gas CO2/S_T ratios reveal dual source of carbon in arc volcanism. Earth-Science Reviews 168, 24–47.https://doi.org/10.1016/j.earscirev.2017.03.005

Aiuppa A., Giudice G., Gurrieri S., Liuzzo M., Burton M., Caltabiano T., McGonigle A. J. S., Salerno G., Shinohara H., Valenza M., 2008. Total volatile flux from Mount Etna. Geophysical Research Letters 35. https://doi.org/10.1029/2008GL035871

Aiuppa, A., Moretti, R., Federico, C., Giudice, G., Gurrieri, S., Liuzzo, M., Papale, P., Shinohara, H., Valenza, M., 2007. Forecasting Etna eruptions by real-time observation of volcanic gas composition. Geology 35, 1115–1118. https://doi.org/10.1130/G24149A.1

Aiuppa Alessandro, Bitetto Marcello, Francofonte Vincenzo, Velasquez Gabriela, Parra Claudia Bucarey, Giudice Gaetano, Liuzzo Marco, Moretti Roberto, Moussallam Yves, Peters Nial, Tamburello Giancarlo, Valderrama Oscar. A., Curtis Aaron, 2017. A CO2‐gas precursor to the March 2015 Villarrica volcano eruption. Geochemistry, Geophysics, Geosystems 18, 2120–2132. https://doi.org/10.1002/2017GC006892

Aiuppa Alessandro, Burton Mike, Caltabiano Tommaso, Giudice Gaetano, Guerrieri Sergio, Liuzzo Marco, Murè Filippo, Salerno Giuseppe, 2010. Unusually large magmatic CO2 gas

emissions prior to a basaltic paroxysm. Geophysical Research Letters 37. https://doi.org/10.1029/2010GL043837

Bluth, G.J.S., Shannon, J.M., Watson, I.M., Prata, A.J., Realmuto, V.J., 2007. Development of an ultra-violet digital camera for volcanic SO2 imaging. Journal of Volcanology and Geothermal Research 161, 47–56. https://doi.org/10.1016/j.jvolgeores.2006.11.004

Boichu, M., Oppenheimer, C., Tsanev, V. and Kyle, P.R., 2010. High temporal resolution SO_2 flux measurements at Erebus volcano, Antarctica. Journal of Volcanology and Geothermal Research, 190(3-4), 325-336.

Calder, E.S., Harris, A.J.L., Peña, P., Pilger, E., Flynn, L.P., Fuentealba, G., Moreno, H., 2004. Combined thermal and seismic analysis of the Villarrica volcano lava lake, Chile. Revista geológica de Chile 31, 259–272. https://doi.org/10.4067/S0716-02082004000200005

Campion, R., Delgado-Granados, H., Mori, T., 2015. Image-based correction of the light dilution effect for SO2 camera measurements. Journal of Volcanology and Geothermal Research 300, 48–57. https://doi.org/10.1016/j.jvolgeores.2015.01.004

Costa, A., Melnik, O., Sparks, R.S.J., 2007. Controls of conduit geometry and wallrock elasticity on lava dome eruptions. Earth and Planetary Science Letters 260, 137–151. https://doi.org/10.1016/j.epsl.2007.05.024

Costantini, L., Pioli, L., Bonadonna, C., Clavero, J., Longchamp, C., 2011. A Late Holocene explosive mafic eruption of Villarrica volcano, Southern Andes: The Chaimilla deposit. Journal of Volcanology and Geothermal Research 200, 143–158. https://doi.org/10.1016/j.jvolgeores.2010.12.010

Darmawan, H., Walter, T.R., Brotopuspito, K.S., Subandriyo, I Gusti Made Agung Nandaka, 2018. Morphological and structural changes at the Merapi lava dome monitored in 2012–15 using unmanned aerial vehicles (UAVs). Journal of Volcanology and Geothermal Research 349, 256–267. https://doi.org/10.1016/j.jvolgeores.2017.11.006

de Moor J. M., Aiuppa A., Avard G., Wehrmann H., Dunbar N., Muller C., Tamburello G., Giudice G., Liuzzo M., Moretti R., Conde V., Galle B., 2016. Turmoil at Turrialba Volcano (Costa Rica): Degassing and eruptive processes inferred from high‐frequency gas monitoring. Journal of Geophysical Research: Solid Earth 121, 5761–5775. https://doi.org/10.1002/2016JB013150

Di Stefano, G., Romeo, G., Mazzini, A., Iarocci, A., Hadi, S., Pelphrey, S., 2018. The Lusi drone: A multidisciplinary tool to access extreme environments. Marine and Petroleum Geology, 10 years of Lusi eruption - lessons learned about modern and ancient piercement systems 90, 26–37. https://doi.org/10.1016/j.marpetgeo.2017.07.006

Diaz, J.A., Pieri, D., Wright, K., Sorensen, P., Kline-Shoder, R., Arkin, C.R., Fladeland, M., Bland, G., Buongiorno, M.F., Ramirez, C., Corrales, E., Alan, A., Alegria, O., Diaz, D., Linick, J., 2015. Unmanned Aerial Mass Spectrometer Systems for In-Situ Volcanic Plume Analysis. J. Am. Soc. Mass Spectrom. 26, 292–304. https://doi.org/10.1007/s13361-014-1058-x

Edmonds, M., Herd, R.A., Galle, B., Oppenheimer, C.M., 2003a. Automated, high time-resolution measurements of SO_2 flux at Soufrière Hills Volcano, Montserrat. Bull Volcanol 65, 578–586. https://doi.org/10.1007/s00445-003-0286-x

Edmonds, M., Oppenheimer, C., Pyle, D.M., Herd, R.A., Thompson, G., 2003b. SO2 emissions from Soufrière Hills Volcano and their relationship to conduit permeability, hydrothermal interaction and degassing regime. Journal of Volcanology and Geothermal Research 124, 23–43. https://doi.org/10.1016/S0377-0273(03)00041-6

Favalli, M., Fornaciai, A., Nannipieri, L., Harris, A., Calvari, S., Lormand, C., 2018. UAV-based remote sensing surveys of lava flow fields: a case study from Etna's 1974 channel-fed lava flows. Bull Volcanol 80, 29. https://doi.org/10.1007/s00445-018-1192-6

Flower, V.J.B., Carn, S.A., 2015. Characterising volcanic cycles at Soufriere Hills Volcano, Montserrat: Time series analysis of multi-parameter satellite data. Journal of Volcanology and Geothermal Research 304, 82–93. https://doi.org/10.1016/j.jvolgeores.2015.07.035

Galle, B., Johansson, M., Rivera, C., Zhang, Y., Kihlman, M., Kern, C., Lehmann, T., Platt, U., Arellano, S., Hidalgo, S., 2010. Network for Observation of Volcanic and Atmospheric Change (NOVAC)—A global network for volcanic gas monitoring: Network layout and instrument description. Journal of Geophysical Research: Atmospheres 115. https://doi.org/10.1029/2009JD011823

Hickey‐Vargas, R., L. López‐Escobar, H. Moreno, J. Clavero, L. Lara, and M. Sun, 2004, Magmatic evolution of the villarrica volcano, in Villarrica Volcano (39.5°S), Southern Andes, Chile, Bol. 61, pp. 39–45, edited by L. E. Lara, and J. Clavero, Serv. Nac. de Geol. y Miner., Santiago, Chile.

Hashimoto, T., Koyama, T., Kaneko, T., Ohminato, T., Yanagisawa, T., Yoshimoto, M., Suzuki, E., 2014. Aeromagnetic survey using an unmanned autonomous helicopter over Tarumae Volcano, northern Japan. Exploration Geophysics 45, 37–42. https://doi.org/10.1071/EG12087

Hickey-Vargas, R., Sun, M., López-Escobar, L., Moreno-Roa, H., Reagan, M.K., Morris, J.D., Ryan, J.G., 2002. Multiple subduction components in the mantle wedge: Evidence from eruptive centers in the Central Southern volcanic zone, Chile. Geology 30, 199–202. https://doi.org/10.1130/0091-7613

Holland, A.P., Watson, I.M., Phillips, J.C., Caricchi, L. and Dalton, M.P., 2011. Degassing processes during lava dome growth: Insights from Santiaguito lava dome, Guatemala. Journal of Volcanology and Geothermal Research, 202(1-2), 153-166.

Horton, K.A., Williams-Jones, G., Garbeil, H., Elias, T., Sutton, A.J., Mouginis-Mark, P., Porter, J.N., Clegg, S., 2006. Real-time measurement of volcanic SO2 emissions: validation of a new UV correlation spectrometer (FLYSPEC). Bull Volcanol 68, 323–327. https://doi.org/10.1007/s00445-005-0014-9

Ilanko, T., Oppenheimer, C., Burgisser, A., Kyle, P., 2015. Cyclic degassing of Erebus volcano, Antarctica. Bull Volcanol 77, 56. https://doi.org/10.1007/s00445-015-0941-z

Jacques, G., Hoernle, K., Gill, J., Hauff, F., Wehrmann, H., Garbe-Schönberg, D., van den Bogaard, P., Bindeman, I., Lara, L.E., 2013. Across-arc geochemical variations in the Southern Volcanic Zone, Chile (34.5–38.0°S): Constraints on mantle wedge and slab input compositions. Geochimica et Cosmochimica Acta 123, 218–243. https://doi.org/10.1016/j.gca.2013.05.016

Johnson, J.B., Watson, L.M., Palma, J.L., Dunham, E.M., Anderson, J.F., 2018. Forecasting the Eruption of an Open-Vent Volcano Using Resonant Infrasound Tones. Geophysical Research Letters 45, 2213–2220. https://doi.org/10.1002/2017GL076506

Kaneko, T., Koyama, T., Yasuda, A., Takeo, M., Yanagisawa, T., Kajiwara, K., Honda, Y., 2011. Low-altitude remote sensing of volcanoes using an unmanned autonomous helicopter: an example of aeromagnetic observation at Izu-Oshima volcano, Japan. International Journal of Remote Sensing 32, 1491–1504. https://doi.org/10.1080/01431160903559770

Kantzas, E.P., McGonigle, A.J.S., Tamburello, G., Aiuppa, A., Bryant, R.G., 2010. Protocols for UV camera volcanic SO2 measurements. Journal of Volcanology and Geothermal Research 194, 55–60. https://doi.org/10.1016/j.jvolgeores.2010.05.003

Kelly, P., 2017. On the accuracy and precision of multi-GAS measurements, Proc. 13th CCVG-IAVCEI gas workshop, Ecuador.

Koyama, T., Kaneko, T., Ohminato, T., Yanagisawa, T., Watanabe, A., Takeo, M., 2013. An aeromagnetic survey of Shinmoe-dake volcano, Kirishima, Japan, after the 2011 eruption using an unmanned autonomous helicopter. Earth Planet Sp 65, 16. https://doi.org/10.5047/eps.2013.03.005

Lamb, O.D., Varley, N.R., Mather, T.A., Pyle, D.M., Smith, P.J., Liu, E.J., 2014. Multiple timescales of cyclical behaviour observed at two dome-forming eruptions. Journal of Volcanology and Geothermal Research 284, 106–121. https://doi.org/10.1016/j.jvolgeores.2014.07.013

Mason, E., Edmonds, M., Turchyn, A.V., 2017. Remobilization of crustal carbon may dominate volcanic arc emissions. Science 357, 290–294. https://doi.org/10.1126/science.aan5049

Mather T. A., Tsanev V. I., Pyle D. M., McGonigle A. J. S., Oppenheimer C., Allen A. G., 2004. Characterization and evolution of tropospheric plumes from Lascar and Villarrica volcanoes, Chile. Journal of Geophysical Research: Atmospheres 109. https://doi.org/10.1029/2004JD004934

McGonigle A. J. S., Aiuppa A., Giudice G., Tamburello G., Hodson A. J., Gurrieri S., 2008. Unmanned aerial vehicle measurements of volcanic carbon dioxide fluxes. Geophysical Research Letters 35. https://doi.org/10.1029/2007GL032508

McGonigle A. J. S., Oppenheimer C., Hayes A. R., Galle B., Edmonds M., Caltabiano T., Salerno G., Burton M., Mather T. A., 2003. Sulphur dioxide fluxes from Mount Etna, Vulcano, and Stromboli measured with an automated scanning ultraviolet spectrometer. Journal of Geophysical Research: Solid Earth 108. https://doi.org/10.1029/2002JB002261

McGonigle, A.J.S., Pering, T.D., Wilkes, T.C., Tamburello, G., D'Aleo, R., Bitetto, M., Aiuppa, A., Willmott, J.R., 2017. Ultraviolet Imaging of Volcanic Plumes: A New Paradigm in Volcanology. Geosciences 7, 68. https://doi.org/10.3390/geosciences7030068

McGonigle, A.J.S., Oppenheimer, C., Galle, B., Mather, T.A., Pyle, D.M., 2002. Walking traverse and scanning DOAS measurements of volcanic gas emission rates. Geophysical Research Letters 29, 46-1-46–4. https://doi.org/10.1029/2002GL015827

Moffat, A.J., Millan, M.M., 1971. The applications of optical correlation techniques to the remote sensing of SO2 plumes using sky light. Atmospheric Environment (1967) 5, 677–690. https://doi.org/10.1016/0004-6981(71)90125-9

Mori, T., Burton, M., 2006. The SO2 camera: A simple, fast and cheap method for ground-based imaging of SO2 in volcanic plumes. Geophysical Research Letters 33. https://doi.org/10.1029/2006GL027916

Moreno, H., J. Clavero, and L. Lara (1994), Explosive post-glacial activity of Villarrica volcano, southern Andes, paper presented at 7th Congreso Geologico Chileno, Univ. of Concepcion, Concepcion, Chile.

Mori, T., Hashimoto, T., Terada, A., Yoshimoto, M., Kazahaya, R., Shinohara, H., Tanaka, R., 2016. Volcanic plume measurements using a UAV for the 2014 Mt. Ontake eruption. Earth Planet Sp 68, 49. https://doi.org/10.1186/s40623-016-0418-0

Morlet, J., Arens, G., Fourgeau, E., Glard, D., 1982. Wave propagation and sampling theory—Part I: Complex signal and scattering in multilayered media. GEOPHYSICS 47, 203–221. https://doi.org/10.1190/1.1441328

Moussallam, Y., Bani, P., Curtis, A., Barnie, T., Moussallam, M., Peters, N., Schipper, C.I., Aiuppa, A., Giudice, G., Amigo, Á., Velasquez, G., Cardona, C., 2016. Sustaining persistent lava lakes: Observations from high-resolution gas measurements at Villarrica volcano, Chile. Earth and Planetary Science Letters 454, 237–247. https://doi.org/10.1016/j.epsl.2016.09.012

Moussallam, Y., Tamburello, G., Peters, N., Apaza, F., Schipper, C.I., Curtis, A., Aiuppa, A., Masias, P., Boichu, M., Bauduin, S., Barnie, T., Bani, P., Giudice, G., Moussallam, M., 2017. Volcanic gas emissions and degassing dynamics at Ubinas and Sabancaya volcanoes; implications for the volatile budget of the central volcanic zone. Journal of Volcanology and Geothermal Research 343, 181–191. https://doi.org/10.1016/j.jvolgeores.2017.06.027

Müller, D., Walter, T.R., Schöpa, A., Witt, T., Steinke, B., Gudmundsson, M.T., Dürig, T., 2017. High-Resolution Digital Elevation Modeling from TLS and UAV Campaign Reveals Structural Complexity at the 2014/2015 Holuhraun Eruption Site, Iceland. Front. Earth Sci. 5. https://doi.org/10.3389/feart.2017.00059

Nakano, T., Kamiya, I., Tobita, M., Iwahashi, J., Nakajima, H., 2014. Landform monitoring in active volcano by UAV and SfM-MVS technique, in: The International Archives of Photogrammetry, Remote Sensing and Spatial Information Sciences; Gottingen. Copernicus GmbH, Gottingen, Germany, Gottingen, pp. 71–75. http://dx.doi.org/10.5194/isprsarchives-XL-8-71-2014

Nicholson, E.J., Mather, T.A., Pyle, D.M., Odbert, H.M., Christopher, T., 2013. Cyclical patterns in volcanic degassing revealed by SO2 flux timeseries analysis: An application to Soufrière Hills Volcano, Montserrat. Earth and Planetary Science Letters 375, 209–221. https://doi.org/10.1016/j.epsl.2013.05.032

Odbert, H.M., Stewart, R.C., Wadge, G., 2014. Chapter 2 Cyclic phenomena at the Soufrière Hills Volcano, Montserrat. Geological Society, London, Memoirs 39, 41–60. https://doi.org/10.1144/M39.2

Odbert, H.M., Wadge, G., 2009. Time series analysis of lava flux. Journal of Volcanology and Geothermal Research 188, 305–314. https://doi.org/10.1016/j.jvolgeores.2009.09.005

Oppenheimer, C., Francis, P., Stix, J., 1998. Depletion rates of sulfur dioxide in tropospheric volcanic plumes. Geophysical Research Letters 25, 2671–2674. https://doi.org/10.1029/98GL01988

OVDAS Reporte Especial de Actividad Volcánica, Región de La Araucanía y Los Ríos, 05 December 2017, 09:50.

Palma José Luis, Calder Eliza S., Basualto Daniel, Blake Stephen, Rothery David A., 2008. Correlations between SO2 flux, seismicity, and outgassing activity at the open vent of Villarrica volcano, Chile. Journal of Geophysical Research: Solid Earth 113. https://doi.org/10.1029/2008JB005577

Parejas, C.S., Druitt, T.H., Robin, C., Moreno, H., Naranjo, J.-A., 2010. The Holocene Pucón eruption of Volcán Villarrica, Chile: deposit architecture and eruption chronology. Bull Volcanol 72, 677–692. https://doi.org/10.1007/s00445-010-0348-9

Percival, D.B., Walden, A.T., 2006. Wavelet Methods for Time Series Analysis. Cambridge University Press.

Percival, D.B., Walden, A.T., 1993. Spectral Analysis for Physical Applications. Cambridge University Press.

Pering, T.D., Tamburello, G., McGonigle, A.J.S., Aiuppa, A., Cannata, A., Giudice, G., Patanè, D., 2014. High time resolution fluctuations in volcanic carbon dioxide degassing from Mount Etna. Journal of Volcanology and Geothermal Research 270, 115–121. https://doi.org/10.1016/j.jvolgeores.2013.11.014

Pering, T.D., Tamburello, G., McGonigle, A.J.S., Hanna, E., Aiuppa, A., 2014. Correlation of oscillatory behaviour in Matlab using wavelets. Computers & Geosciences 70, 206–212. https://doi.org/10.1016/j.cageo.2014.06.006

Pering, T.D., Tamburello, G., McGonigle, A.J.S., Aiuppa, A., James, M.R., Lane, S.J., Sciotto, M., Cannata, A., Patanè, D., 2015. Dynamics of mild strombolian activity on Mt. Etna. Journal of Volcanology and Geothermal Research 300, 103–111. https://doi.org/10.1016/j.jvolgeores.2014.12.013

Peters, N. and Oppenheimer, C., 2018. Plumetrack: Flux calculation software for UV cameras. Computers & Geosciences 118, 86-90. https://doi.org/10.1016/j.cageo.2018.05.014

Peters, N., Hoffmann, A., Barnie, T., Herzog, M., Oppenheimer, C., 2015. Use of motion estimation algorithms for improved flux measurements using SO2 cameras. Journal of Volcanology and Geothermal Research 300, 58–69. https://doi.org/10.1016/j.jvolgeores.2014.08.031

Pieri, D., Diaz, J.A., Bland, G., Fladeland, M., Madrigal, Y., Corrales, E., Alegria, O., Alan, A., Realmuto, V., Miles, T., Abtahi, A., 2013. In situ observations and sampling of volcanic emissions with NASA and UCR unmanned aircraft, including a case study at Turrialba Volcano, Costa Rica. Geological Society, London, Special Publications 380, 321–352. https://doi.org/10.1144/SP380.13

Platt, U., Bobrowski, N., Butz, A., Platt, U., Bobrowski, N., Butz, A., 2018. Ground-Based Remote Sensing and Imaging of Volcanic Gases and Quantitative Determination of Multi-Species Emission Fluxes. Geosciences 8, 44. https://doi.org/10.3390/geosciences8020044

Richardson, J.P., Waite, G.P., Palma, J.L., 2014. Varying seismic-acoustic properties of the fluctuating lava lake at Villarrica volcano, Chile. Journal of Geophysical Research: Solid Earth 119, 5560–5573. https://doi.org/10.1002/2014JB011002

Roberts, T.J., Lurton, T., Giudice, G., Liuzzo, M., Aiuppa, A., Coltelli, M., Vignelles, D., Salerno, G., Couté, B., Chartier, M., Baron, R., Saffell, J.R., Scaillet, B., 2017. Validation of a novel Multi-Gas sensor for volcanic HCl alongside H_2S and SO_2 at Mt. Etna. Bull Volcanol 79, 36. https://doi.org/10.1007/s00445-017-1114-z

Rüdiger, J., Tirpitz, J.-L., de Moor, J.M., Bobrowski, N., Gutmann, A., Liuzzo, M., Ibarra, M., Hoffmann, T., 2018. Implementation of electrochemical, optical and denuder-based sensors and sampling techniques on UAV for volcanic gas measurements: examples from Masaya, Turrialba and Stromboli volcanoes. Atmospheric Measurement Techniques; Katlenburg-Lindau 11, 2441–2457. http://dx.doi.org/10.5194/amt-11-2441-2018

Santoro, S., Parracino, S., Fiorani, L., D'Aleo, R., Di Ferdinando, E., Giudice, G., Maio, G., Nuvoli, M., Aiuppa, A., 2017. Volcanic Plume CO2 Flux Measurements at Mount Etna by Mobile Differential Absorption Lidar. Geosciences 7, 9. https://doi.org/10.3390/geosciences7010009

Sawyer, G.M., Salerno, G.G., Le Blond, J.S., Martin, R.S., Spampinato, L., Roberts, T.J., Mather, T.A., Witt, M.L.I., Tsanev, V.I., Oppenheimer, C., 2011. Gas and aerosol emissions from Villarrica volcano, Chile. Journal of Volcanology and Geothermal Research 203, 62–75. https://doi.org/10.1016/j.jvolgeores.2011.04.003

Shinohara, H., 2013. Composition of volcanic gases emitted during repeating Vulcanian eruption stage of Shinmoedake, Kirishima volcano, Japan. Earth Planet Sp 65, 17. https://doi.org/10.5047/eps.2012.11.001

Shinohara, H., 2005. A new technique to estimate volcanic gas composition: plume measurements with a portable multi-sensor system. Journal of Volcanology and Geothermal Research 143, 319–333. https://doi.org/10.1016/j.jvolgeores.2004.12.004

Shinohara H., Aiuppa A., Giudice G., Gurrieri S., Liuzzo M., 2008. Variation of H2O/CO2 and CO2/SO2 ratios of volcanic gases discharged by continuous degassing of Mount Etna volcano, Italy. Journal of Geophysical Research: Solid Earth 113. https://doi.org/10.1029/2007JB005185

Shinohara H., Witter J. B., 2005. Volcanic gases emitted during mild Strombolian activity of Villarrica volcano, Chile. Geophysical Research Letters 32. https://doi.org/10.1029/2005GL024131

Stix, J., Moor, J.M. de, Rüdiger, J., Alan, A., Corrales, E., D'Arcy, F., Diaz, J.A., Liotta, M., 2018. Using Drones and Miniaturized Instrumentation to Study Degassing at Turrialba and Masaya Volcanoes, Central America. Journal of Geophysical Research: Solid Earth 0. https://doi.org/10.1029/2018JB015655

Tamburello, G., 2015. Ratiocalc: Software for processing data from multicomponent volcanic gas analyzers. Computers & Geosciences 82, 63–67. https://doi.org/10.1016/j.cageo.2015.05.004

Tamburello, G., Aiuppa, A., Kantzas, E.P., McGonigle, A.J.S., Ripepe, M., 2012. Passive vs. active degassing modes at an open-vent volcano (Stromboli, Italy). Earth and Planetary Science Letters 359–360, 106–116. https://doi.org/10.1016/j.epsl.2012.09.050

Tamburello G., Aiuppa A., McGonigle A. J. S., Allard P., Cannata A., Giudice G., Kantzas E. P., Pering T. D., 2013. Periodic volcanic degassing behavior: The Mount Etna example. Geophysical Research Letters 40, 4818–4822. https://doi.org/10.1002/grl.50924

Thompson, D., 1982. Spectrum estimation and harmonic analysis. Proc. IEEE 70, 1055–1096.

Torrence, C., Compo, G.P., 1998. A Practical Guide to Wavelet Analysis. Bull. Amer. Meteor. Soc. 79, 61–78. https://doi.org/10.1175/1520-0477

Turner, N.R., Perroy, R.L., Hon, K., 2017. Lava flow hazard prediction and monitoring with UAS: a case study from the 2014–2015 Pāhoa lava flow crisis, Hawai‘i. Journal of Applied Volcanology 6, 17. https://doi.org/10.1186/s13617-017-0068-3

Werner C., Hurst T., Scott B., Sherburn S., Christenson B. W., Britten K., Cole‐Baker J., Mullan B., 2008. Variability of passive gas emissions, seismicity, and deformation during crater lake growth at White Island Volcano, New Zealand, 2002–2006. Journal of Geophysical Research: Solid Earth 113. https://doi.org/10.1029/2007JB005094

Wehrmann, H., Hoernle, K., Jacques, G., Garbe-Schönberg, D., Schumann, K., Mahlke, J., Lara, L.E., 2014. Volatile (sulphur and chlorine), major, and trace element geochemistry of mafic to intermediate tephras from the Chilean Southern Volcanic Zone (33–43°S). Int J Earth Sci (Geol Rundsch) 103, 1945–1962. https://doi.org/10.1007/s00531-014-1006-9

Weibring, P., Edner, H., Svanberg, S., Cecchi, G., Pantani, L., Ferrara, R., Caltabiano, T., 1998. Monitoring of volcanic sulphur dioxide emissions using differential absorption lidar (DIAL), differential optical absorption spectroscopy (DOAS), and correlation spectroscopy (COSPEC). Appl Phys B 67, 419–426. https://doi.org/10.1007/s003400050525

Wilkes, T.C., McGonigle, A.J.S., Pering, T.D., Taggart, A.J., White, B.S., Bryant, R.G., Willmott, J.R., 2016. Ultraviolet Imaging with Low Cost Smartphone Sensors: Development and Application of a Raspberry Pi-Based UV Camera. Sensors 16, 1649. https://doi.org/10.3390/s16101649

Wilkes, T.C., Pering, T.D., McGonigle, A.J.S., Tamburello, G., Willmott, J.R., 2017. A Low-Cost Smartphone Sensor-Based UV Camera for Volcanic SO2 Emission Measurements. Remote Sensing 9, 27. https://doi.org/10.3390/rs9010027

Witter, J.B., Delmelle, P., 2004. Acid gas hazards in the crater of Villarrica volcano (Chile). Revista geológica de Chile 31, 273–277. https://doi.org/10.4067/S0716-02082004000200006

Xi, X., Johnson, M.S., Jeong, S., Fladeland, M., Pieri, D., Diaz, J.A., Bland, G.L., 2016. Constraining the sulfur dioxide degassing flux from Turrialba volcano, Costa Rica using

unmanned aerial system measurements. Journal of Volcanology and Geothermal Research 325, 110–118. https://doi.org/10.1016/j.jvolgeores.2016.06.023

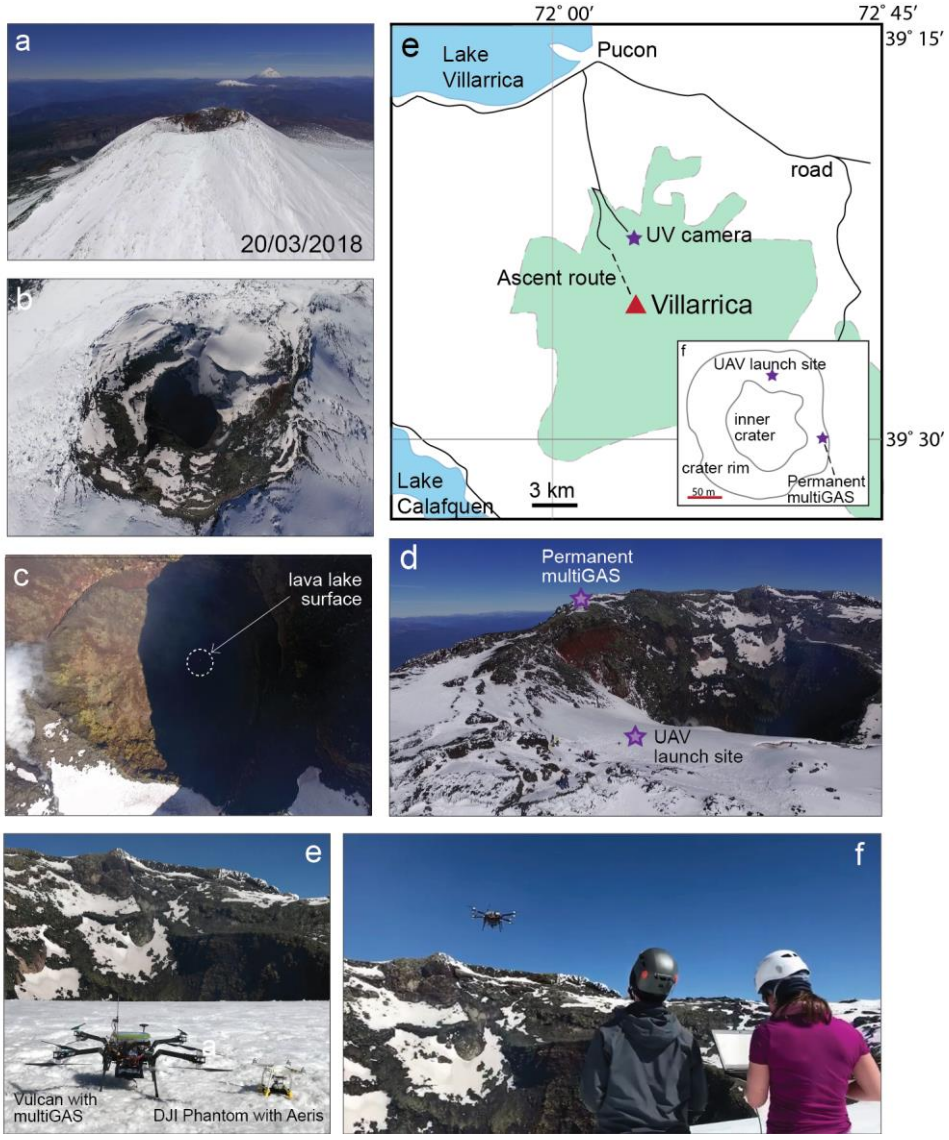

Figure 1: Location and volcanological setting; (a) Volcán Villarrica is the easternmost in a chain of three volcanoes (Lanin, Quetrapillan) striking obliquely to the main N-S axis of volcanism; (b, c) The magma level was extremely low in the conduit during the measurement campaign, with the lake surface only visible as several pixels in aerial imagery; (d) UAS were launched from a sheltered plateau on the northern rim of the crater, with the semi-permanent multi-GAS station visible on the eastern rim; (e) Location map of the region, showing the position of UV camera. The green shaded region delimits the extent of the national park. Inset: Aerial map of the summit region shown in (d). The summit crater is ~200 m in diameter; (e) Two instrumented multi-rotor vehicles were used in this campaign, the Vulcan octocopter with multi-GAS (left) and DJI Phantom 3 Pro with Aeris gas sensor (right); (f) Vulcan UAS in flight on 20/03/18.

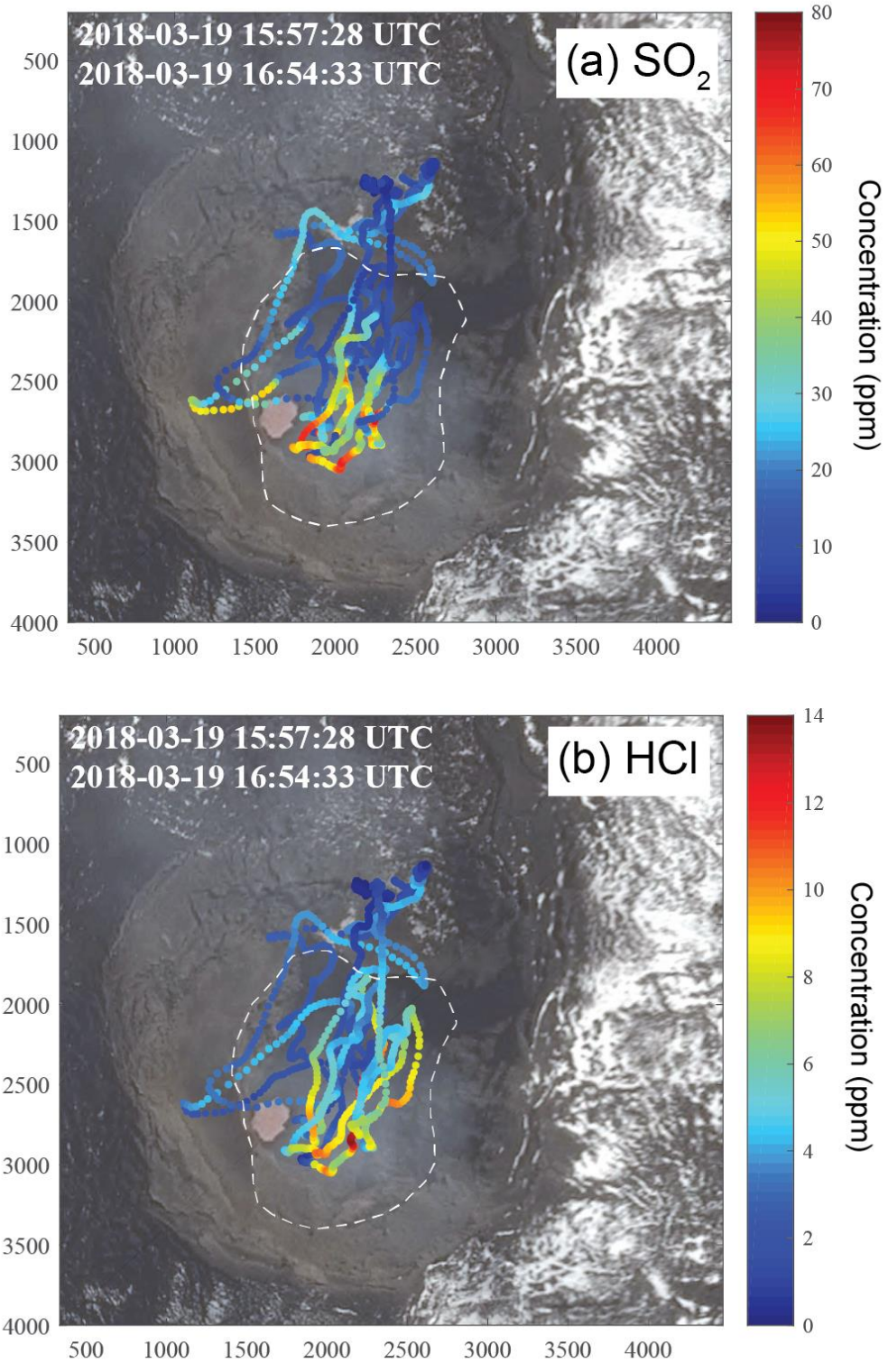

Figure 2: Cross-sectional plume maps of (a) SO_2 and (b) HCl concentrations measured between 15:57 UTC and 16:54 UTC on 20/03/2018. Each datapoint represents a discrete gas measurement every 0.8 seconds, positioned using co-recorded GPS location and coloured according to concentration. Dashed lines delimit the crater area.

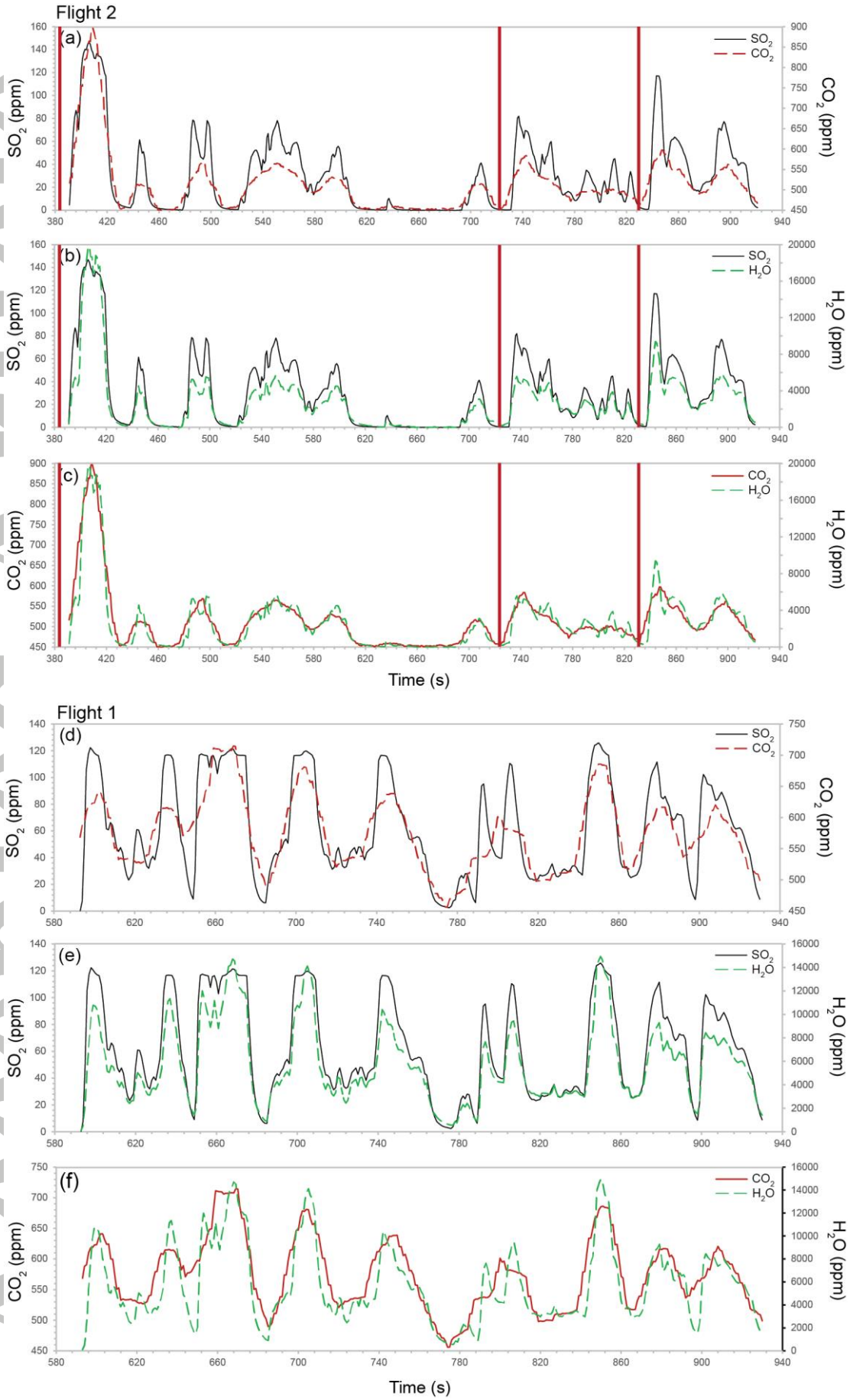

Figure 3: Concentration timeseries for (a–c) multi-GAS Flight V1 at 16:49:00 UTC on 21/03/2018 showing co-variation between multiple gas species; (a) SO_2 and CO_2; (b) SO_2 and H_2O; and (c) CO_2 and H_2O. Measurement uncertainties on individual SO_2 and CO_2 values are 1 ppm ± 2% of the signal. Vertical red lines indicate the timing of audible gas exhalations recorded during the flight. Note that although the behaviour was clearly heard and observed between flights, it was difficult to hear the exhalations above the motor noise from the UAV, so many events were unrecorded. **(d–f) Multi-GAS Flight V2** at 18:08:30 UTC on 21/03/2018 showing co-variation between multiple gas species; (d) SO_2 and CO_2; (e) SO_2 and H_2O; and (f) CO_2 and H_2O. Measurement uncertainties on individual SO_2 and CO_2 values are 1 ppm ± 2% of the signal.

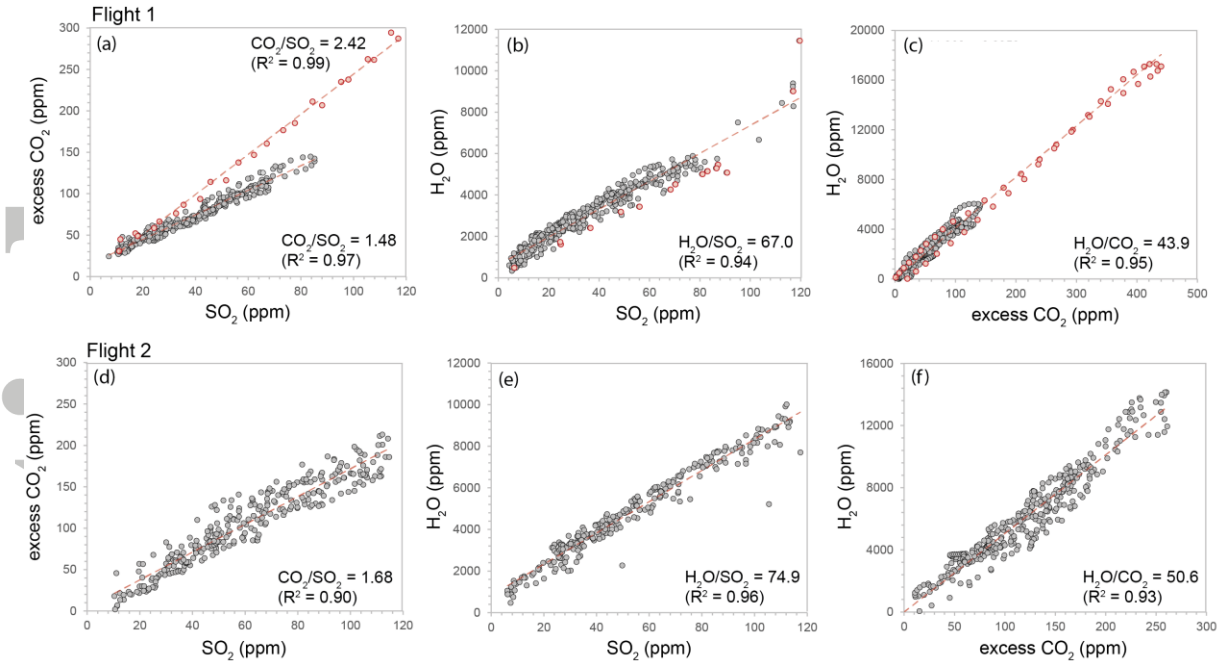

Figure 4: Molar ratios of gas species for (a, b, c) Flight V1, and (d, e, f) Flight V2. Ratios are determined from the slope of the best-fitting linear regression line. Only data where SO_2 is >10 ppmv and <120 ppmv SO_2 were used for the regression. Samples outside of these limits were excluded from the regression and are not displayed. Red symbols in (a-c) highlight an individual gas pulse that is characterised by an apparently more CO_2-rich composition. However, molar gas ratios are based on regression of the grey symbols only, as the anomalous gas pulse is not representative of the degassing characteristics during the measurement interval. Uncertainties on derived molar ratios are 6–12%, based on laboratory tests conducted at INGV Palermo.

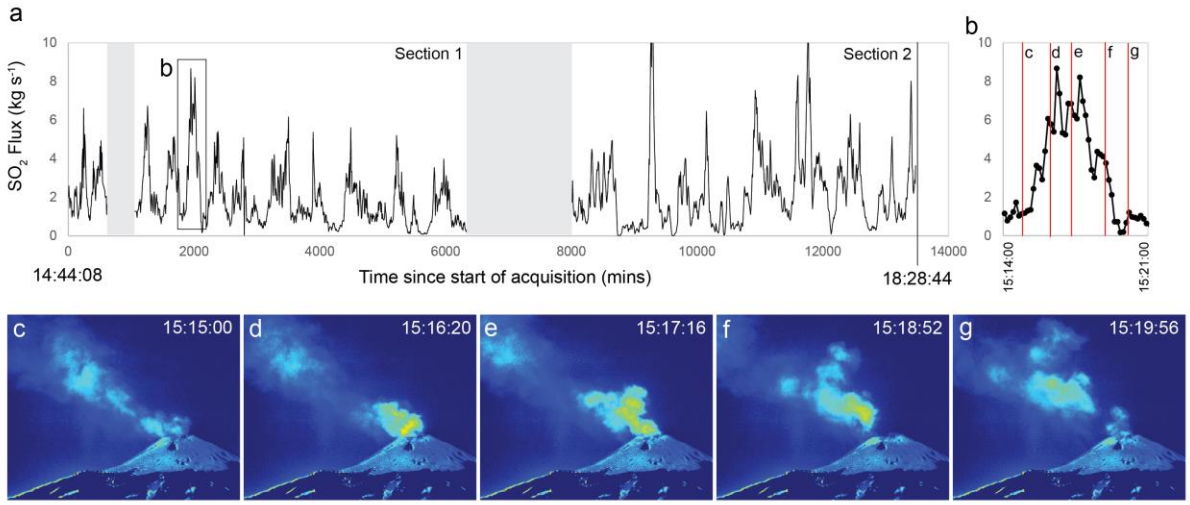

Figure 5: SO_2 flux timeseries; (a) Timeseries of SO_2 flux from 14:44:04 to 18:28:44 UTC (3hrs 45mins) on 25 March 2018, derived from UV camera-generated integrated column amounts multiplied by plume speeds calculated using optical flow algorithms (Peters et al., 2015). Shaded regions correspond to breaks in acquisition during re-calibration of the camera; (b) Magnified view of a section of the SO_2 flux timeseries showing an individual gas 'puff'; (c–f) Time-stamped absorbance images showing the evolution of an individual gas 'puff'. The acquisition times of the images (c–f) correspond to the red vertical lines displayed on (b).

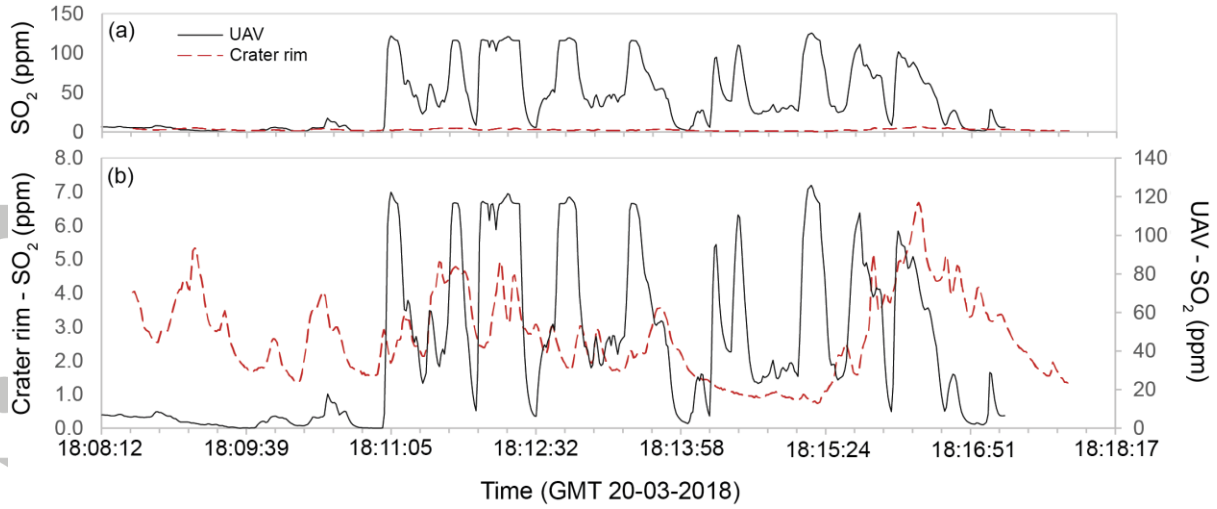

Figure 6: Comparison between contemporaneous proximal UAS and crater rim SO_2 measurements; (a) Same scaled axis highlights the magnitude of plume dilution between the proximal measurements directly above the conduit and the crater rim only 100 m downwind; (b) Timeseries displayed on individually scaled axes to compare the fine-scale detail. Even considering the temporal offset imposed by the downwind travel time, the periodic component of the proximal UAS trace is indistinguishable in the crater rim data.

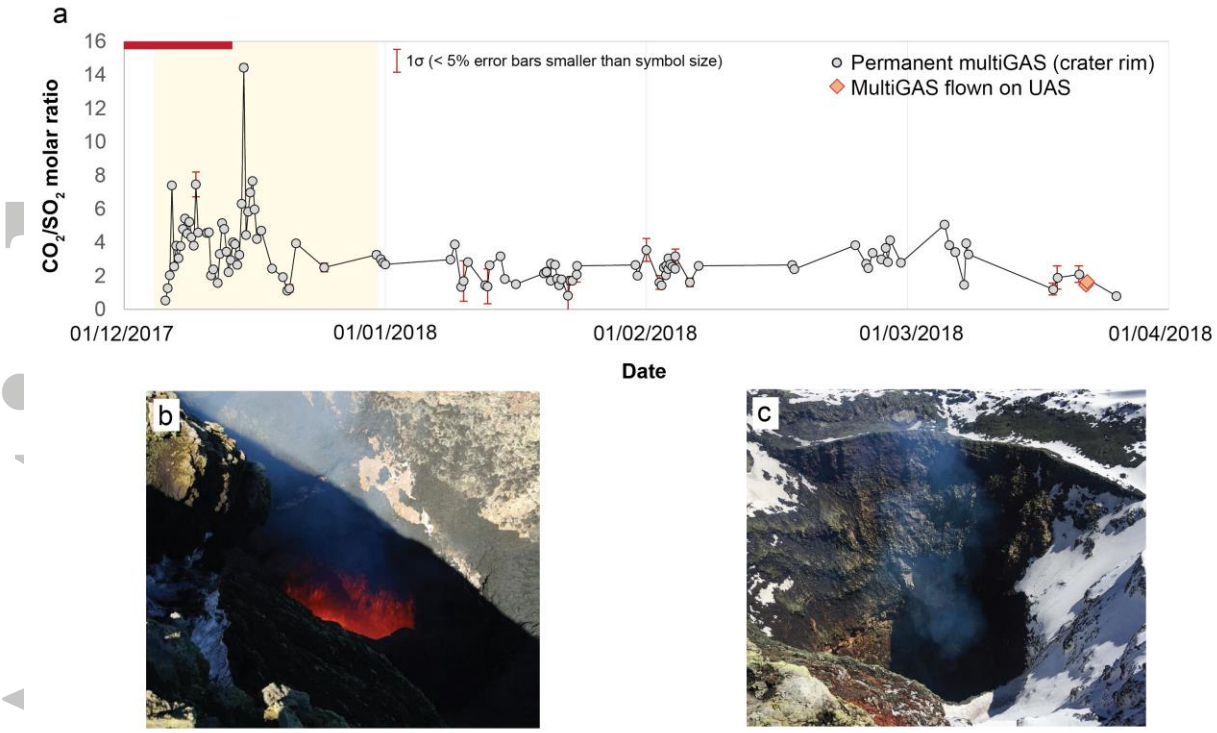

Figure 7: Long-term timeseries of CO_2/SO_2 molar ratios at Villarrica; Molar ratios are derived from raw CO_2 and SO_2 concentrations (measured by a permanent, automated multi-GAS station on the eastern crater rim of Villarrica; grey circles) using RatioCalc software (Tamburello, 2015); each datapoint represents the average CO_2/SO_2 ratio within a 30-minute acquisition window. Molar ratios derived from concentration timeseries acquired by the UAS-based multi-GAS are shown as orange symbols. Error bars represent the standard error of the regression for each acquisition window; errors < 5% are smaller than the size of the symbol. The shaded yellow region shows the period where the alert level defined by OVDAS was raised to yellow alert (from green). The red solid bar highlights the period where the lava lake surface was visible from the crater rim; it retreated abruptly below sight in mid-December 2017.

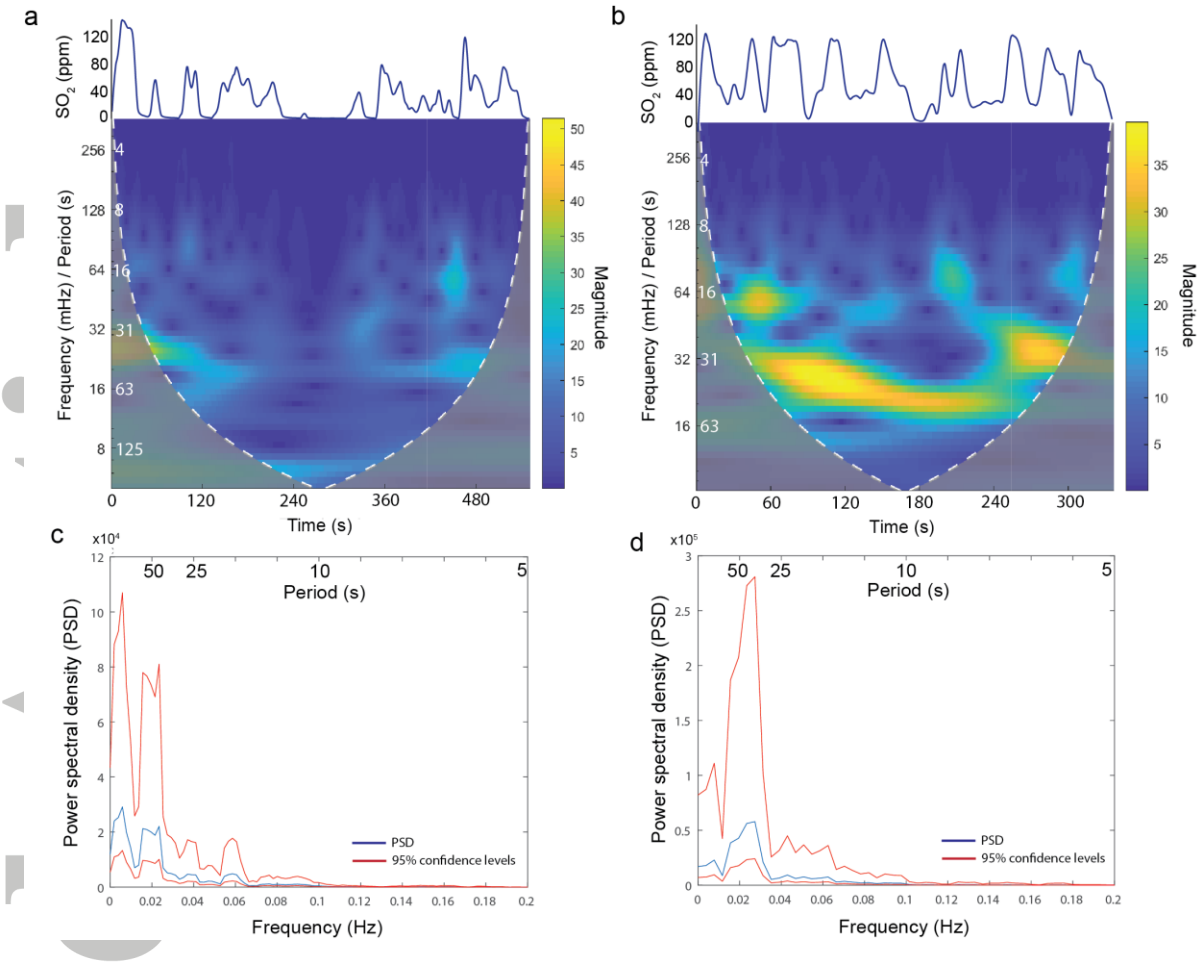

Figure 8: Periodic behaviour in SO_2 concentration timeseries; Continuous wavelet transform (CWT) scalograms for (a) Flight V1 and (b) V2), showing the magnitude of wavelet coefficients resulting from convolution of the SO_2 timeseries with scaled (y-axis) and shifted (x-axis) versions of the Morlet wavelet. Note the different range of magnitudes shown by the colour-scale for each flight. The shaded region represents the wavelet-specific cone-of-influence (COI), which highlights the region of the CWT scalogram potentially affected by edge effects. The filtered timeseries of SO_2 concentration is shown above for comparison; (c, d) Multi-taper Method Fast Fourier Transform (MTM-FFT) spectra showing the power spectral density (PSD) at each frequency <0.2 Hz. The red lines indicate the upper and lower 95% confidence intervals.

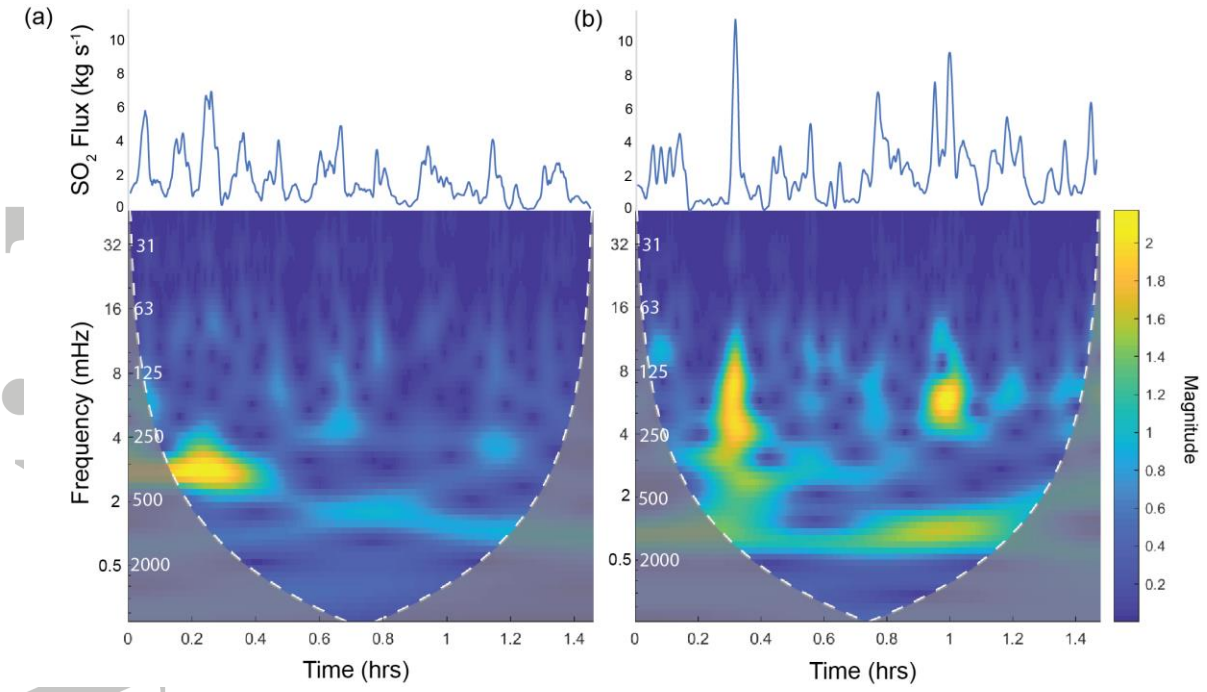

Figure 9: Periodic behaviour in SO_2 flux derived from UV camera images; Continuous wavelet transform (CWT) scalograms for (a) section 2 and (b) section 3 of the SO_2 flux timeseries (shown in Figure 8a) illustrating the magnitude of wavelet coefficients resulting from convolution of the flux timeseries with scaled (y-axis) and shifted (x-axis) versions of the Morlet wavelet. The filtered timeseries of SO_2 flux is shown above for comparison. The shaded region represents the wavelet-specific cone-of-influence (COI), which highlights the region of the CWT scalogram potentially affected by edge effects.